

CHEMISTRY

Highly efficient production of nitrite and nitrate from air at the gas-water interface of nanobubbles

Sandeep Bose¹, Saeed Bahadorikhalili², Yuanyi He¹, Hamidreza Samouei², Richard N. Zare^{1*}

We report a simple, one-step conversion of air to nitrogen oxyanions (NO_x^-), i.e., nitrate (NO_3^-) and nitrite (NO_2^-), at the gas-water interface (GWI) of nanobubbles (NBs). The nanobubble generator is placed inside an aqueous solution of $50 \mu\text{M Fe}^{2+}$ to enhance the production of hydroxyl radicals ($\text{OH}\cdot$) by initiating Fenton's reaction at the GWI. The formation of NO_x^- does not require any external potential or radiation. The NO_x^- production rate using NBs is found to be $60.4 \pm 1.21 \mu\text{M hour}^{-1}$, which shows a fourfold increase in the production as compared to the same reaction performed in microbubbles ($15 \mu\text{M hour}^{-1}$), which is the result from an enhanced electric field strength at the GWI. We propose that this nitrogen-fixation approach presents a promising pathway for an eco-friendly, energy-efficient, and scalable solution for NO_x^- -based sustainable fertilizer production.

INTRODUCTION

Nitrate (NO_3^-) is an essential component in fertilizers for plant nutrition and growth (1, 2). The industrial source of NO_3^- required for the manufacturing of fertilizers comes from nitric acid (HNO_3) production (3). Caused by the increasing demand, the global HNO_3 production reached 57 million metric tons (MMT) in 2023 and is projected to reach 70 MMT by 2032 (4). Currently, the majority of HNO_3 is typically produced through the high-temperature catalytic oxidation of ammonia (NH_3) (5). The NH_3 required for the synthesis of HNO_3 is generally produced via the energy-intensive Haber-Bosch process. The process involves carbon dioxide (CO_2) emission, a greenhouse gas from the steam reforming of methane (CH_4) into hydrogen (H_2) to react with (dinitrogen) N_2 (5). Consequently, nitrate production is presently poor for the environment.

Photo/electrocatalytic N_2 oxidation has emerged as a promising, environmentally friendly strategy for NO_3^- production (6–8). However, its practical implementation is hindered by several challenges, including low production rates and suboptimal Faradaic efficiencies (9, 10). These limitations stem from difficulties such as the strong $\text{N}\equiv\text{N}$ bond strength, poor N_2 adsorption, competition from water oxidation, and low solubility of N_2 (10). In addition, issues related to the complicated design of active sites (11), charge carrier recombination (12), and catalyst deactivation (13) further impede the efficiency and broader application of photo/electrocatalysis. Recent studies indicate that N_2 can be oxidized to nitrate (NO_3^-) via an electrocatalytic process that involves Fenton's reaction, where hydroxyl radicals ($\text{OH}\cdot$) are produced through the dissociation of hydrogen peroxide (H_2O_2) (14, 15). However, this conversion process necessitates the application of an external potential, the use of chemicals such as H_2O_2 , and specialized electrodes, all of which complicate the operation and elevate the associated costs. Yang and coworkers (16) have also shown that laser-induced bubbling in a liquid medium can also convert N_2 to NH_3 or NO_3^- without any catalyst, but the required energy is even higher than the traditional Haber-Bosch process. Therefore, a simple, efficient and eco-friendly method for producing NO_3^- is highly desirable.

Water is typically considered a stable and relatively inert molecule in bulk solution. However, its behavior is notably different at the gas-water interface (GWI) of micrometer-sized water droplets (17, 18). The interfaces of microdroplets exhibit unique physicochemical properties, offering a promising platform to facilitate redox reactions and a cascade of radical-driven chemical transformations (19–37). The exceptional behavior at the interface arises from many factors such as strong interfacial electric field (38–40), pH (41), partial solvation (42), solvent evaporation (43), and molecular orientation at the interface (44, 45). This allows the electron transfer between the surface bound OH^- and H^+ ions leading to the generation of $\text{H}\cdot$ and $\text{OH}\cdot$ at the interface. Taking advantage of these factors, Banerjee and coworkers (46) demonstrated the production of nitrogen oxides (HNO_2 and HNO_3) from air using microdroplets. However, the output remains at the parts-per-trillion level due to the short microsecond reaction time and the limited quantity of microdroplets involved. Previous studies by Ciampi and coworkers (47) indicate that microbubbles (MBs) can be as effective as microdroplets in facilitating redox reactions at their interface. Drawing inspiration from these previous studies, Bose *et al.* (48, 49) reported a MB experiment where NO_3^- was generated by passing MBs of N_2 through water with the addition of ferrous ions (Fe^{2+}). H_2O_2 generated at the GWI during microbubbling plays an important role in NO_3^- production by initiating Fenton's reaction at the interface. Although the method does not require application of an external potential or radiation, and no external chemicals such as H_2O_2 were added into the reaction system, the MB generation process requires high energy due to the use of ultrasonication (240 W, 40 kHz) along with a porous MB generator (air stone). Besides, the NO_3^- production rate remained relatively low at $12.9 \mu\text{M hour}^{-1}$.

In this study, we used nanobubbles (NBs) instead of MBs to address the low nitrate (NO_3^-) production rates. Aqueous Fe^{2+} was used to generate $\text{OH}\cdot$ from in situ-produced H_2O_2 at the NB interface. Again, no external voltage or radiation needs to be applied. The NBs were generated using a portable device equipped with porous carbon fiber and connected to a 10-Hz vibrating rod, making the NB generation process energy-efficient with minimal energy consumption. Owing to their smaller size, NBs provide a larger interfacial area and increased curvature (50, 51) causing the electric field at the interface to be enhanced compared to MBs. This results in an

¹Department of Chemistry, Stanford University, Stanford, CA 94305, USA. ²Department of Petroleum Engineering, Texas A&M University, College Station, TX 77843, USA.

*Corresponding author. Email: zare@stanford.edu

accelerated reaction rate at the GWI, leading to an overall increase in N_2 oxidation.

RESULTS

Experimental setup for NB generation

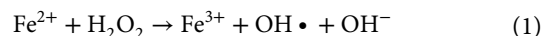
The experimental setup consists of a porous carbon fiber membrane with a diameter ranging from 2 to 9 μm mounted to a rod vibrating at a frequency of ~ 10 Hz (Fig. 1). The function of the vibrating rod is to maintain the homogeneity of the NBs. The nanobubbler was purchased from Environmental Compliance Equipment. The carbon fiber membrane was connected to a gas cylinder (N_2 /air) operating at a gas pressure of 30 psi to generate NBs in the solution. The carbon nanofiber membrane was dipped halfway into a vessel containing 250 ml of aqueous Fe^{2+} solution (50 μM). The carbon nanofiber was positioned in the solution in such a way that it was not in proximity to the container walls, allowing sufficient space for the generated NBs to travel freely through the solution and minimizing their collision with the container walls. Both the container and the carbon nanofiber were clamped to prevent any movement resulting from vibrations. All plastic consumables (tubes, vials, and connectors) were avoided to eliminate any possibility of phthalate leaching that could act as surfactants and stabilize NBs, potentially influencing their chemical activity. Only Teflon tubing was used for gas delivery, as polytetrafluoroethylene (PTFE) is chemically inert and does not readily leach organic compounds into the solution. Thoroughly cleaned and dust-free glassware was used to avoid any contamination. The steel components of the NB generator were also extensively rinsed with ultrapure water to remove any potential residues. Control experiments were performed by purging air into the solution without nanobubbling, both in the presence and in the absence of the nanobubbler. Both shows trace amount of NO_x^- (0.1 μM), which confirms that the steel components did not contribute to NO_x^- formation.

Harnessing NBs for NO_x^- generation

To verify the successful generation of suspended NBs, their sizes were characterized using nanoparticle tracking analysis (NTA). Immediately

after the experiment, the average NB size was determined to be 136.6 ± 3.6 nm (Fig. 2A). As a control, pure water was analyzed without undergoing the bubbling process. No detectable peak was observed in the nanometer range, confirming that NBs were formed exclusively from the bubbling experiment. Both pure water and NB-containing water appeared indistinguishable to the naked eye, as NBs are too small to be visually observed, unlike MBs, which impart a milky appearance to the solution. However, upon exposure to light, the NB suspension exhibited scattering effects that were absent in pure water (fig. S1).

The formation of NBs leads to in situ generation of H_2O_2 at the air-water interface. Upon addition of Fe^{2+} , the H_2O_2 undergoes a Fenton reaction at the gas-NB interface, producing highly reactive $OH\cdot$ as follows



The $OH\cdot$ generated at the interface reacts with the N_2 present in air to form nitrite (NO_2^-) and nitrate (NO_3^-). For clarity, the combined concentration of NO_2^- and NO_3^- is hereafter referred to as NO_x^- . The presence of H_2O_2 in the NB system was first verified using peroxide test strips and subsequently quantified by a potassium titanium oxalate (PTO)-based spectrophotometric assay. As shown in fig. S2, continuous bubbling of air in the presence of Fe^{2+} resulted in a steady accumulation of H_2O_2 over time. After 1 hour, the concentration reached 67 μM , increasing linearly thereafter with a production rate of 56.1 ± 1.8 $\mu\text{M hour}^{-1}$.

Previous electrochemical studies established $OH\cdot$ as the active species in N_2 oxidation to NO_3^- (15). To verify the presence of $OH\cdot$ in our NB system, we analyzed the samples using positive-ion mass spectrometry. The resulting spectrum (fig. S3) exhibited a distinct signal at mass/charge ratio (m/z) 36, corresponding to the hydroxyl radical adduct with hydronium, $[OH\cdot + H_3O]^+$, consistent with earlier reports (52). This provides strong evidence for the generation of $OH\cdot$ within the NBs. Additional signals were observed at m/z 37 and 41, attributable to $[H_2O + H_3O]^+$ and $[H_2O + Na]^+$, respectively. A potential overlap at m/z 36 could arise from $[NH_4OH + H]^+$, which would indicate NH_3 as a product. However, spectrophotometric analysis following Li *et al.* (53) and confirmation with a commercial NH_3 detection kit revealed no evidence of ammonia formation (fig. S4). Furthermore, the Fenton-like environment in our system is strongly oxidative, making the reduction of N_2 to NH_3 thermodynamically unfavorable. Therefore, the m/z 36 peak is conclusively assigned to $[OH\cdot + H_3O]^+$. Water NBs are themselves capable of generating $OH\cdot$. To account for this, we conducted a control experiment in the absence of Fe^{2+} . The mass spectrum still displayed a signal attributable to $OH\cdot$. However, its intensity was relatively weak compared with the much stronger signal observed when Fe^{2+} was present (fig. S3). Because the $OH\cdot$ intensity without Fe^{2+} is so small relative to that with Fe^{2+} , the overall $OH\cdot$ signal essentially reflects the contribution almost entirely from the Fe^{2+} -driven Fenton process.

Continuous NB generation led to a steady, time-dependent rise in the NO_x^- concentration. It is important to note that an activated carbon filter was used to eliminate any HNO_3 impurities from the gas stream (Fig. 1). After 1 hour, the NO_x^- level reached 67.1 μM , and prolonged bubbling for 5 hours caused the concentration to increase to 293.4 μM (Fig. 2B). This appreciable accumulation achieved through extended bubbling highlights the potential of our approach as a simple, eco-friendly, and selective route for large-scale

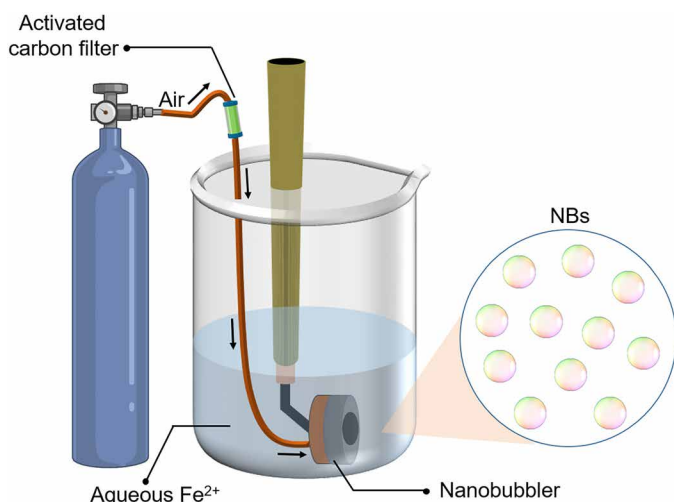


Fig. 1. Schematic of the experimental setup. This is used for NB generation and conversion of N_2 in air to NO_x^- in solution.

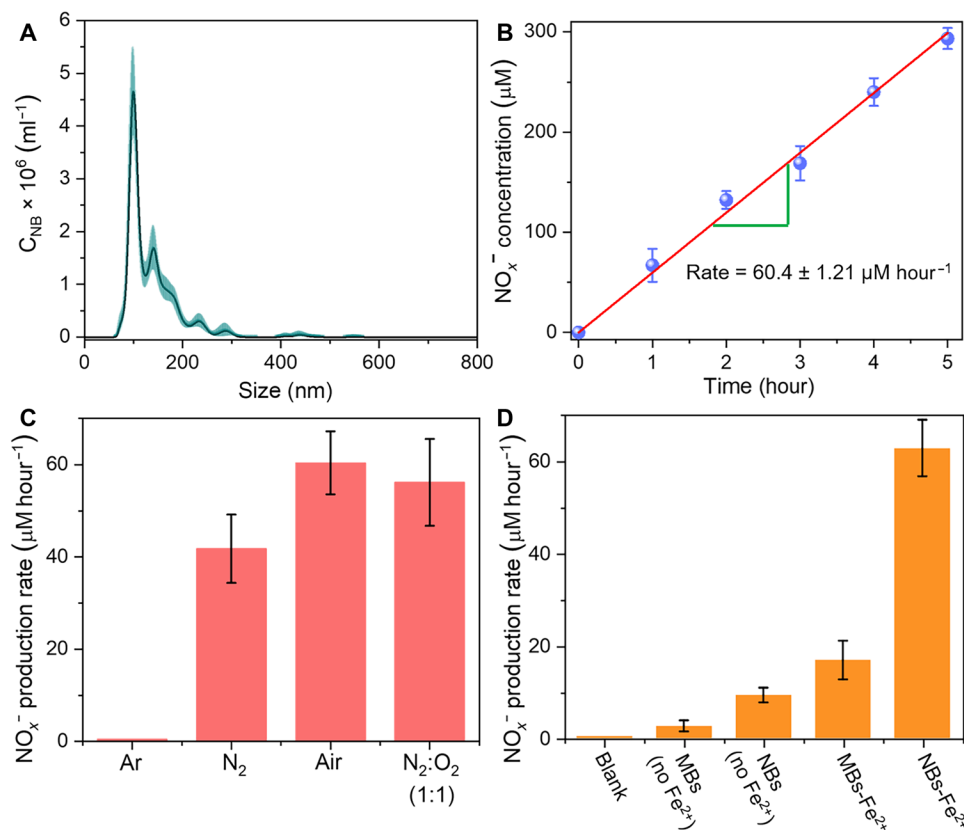


Fig. 2. NO_x⁻ generation at the NB interface. (A) NTA conducted to measure the size of the NBs generated in the solution after bubbling air through the NB generator. Pure water was used as a control to show no NB generation in the absence of bubbling. Average value of five different measurements was plotted along with the SE. (B) The concentration of NO_x⁻ as a function of the air bubbling time. The rate of NO_x⁻ formation was found to be $60.4 \pm 1.21 \mu\text{M hour}^{-1}$. (C) A comparison in the production of NO_x⁻ when the bubbling was performed at different N₂ to O₂ pressure ratio. (D) A comparison of the NO_x⁻ production in the solution when different bubbling methods were used. Each NO_x⁻ experiment was conducted in triplicate, and the average values from the three independent runs are shown in the graph. The associated uncertainties are represented by error bars, which represent one SD.

NO₂⁻/NO₃⁻ production. From these measurements, the NO_x⁻ formation rate was determined to be $60.4 \pm 1.21 \mu\text{M hour}^{-1}$.

To confirm the role of NBs in the chemical transformation, we conducted degassing experiment on the nanobubbled sample. The reaction mixture was first purged with argon gas (Ar) for 15 min and subsequently subjected to vacuum degassing for 30 min. The number density was then measured by NTA. We observed that degassing reduced the NTA-detected number density from 1.8×10^8 to 17.3×10^6 bubbles/ml, indicating sufficient removal of NBs (fig. S5A). Furthermore, the NO_x⁻ concentration was monitored before and after the degassing treatment. For the nondegassed sample, the NO_x⁻ concentration increased notably after 3 hours, whereas the degassed sample showed a minute increase over the same period (fig. S5B). Again, centrifugation of the nanobubbled solution was performed at 4000 rotations per minute (RPM) for 5 min and the supernatant was collected for NTA analysis. We observed a slight decrease in particle density after centrifugation (fig. S5C). This may arise from the coalescence of NBs during centrifugation, producing MBs that subsequently rise and escape due to their higher buoyancy. An alternative explanation is the presence of suspended nanoparticles (impurities) that pellet together under centrifugation. Therefore, we collected the supernatant and the NO_x⁻ concentration was measured along with the uncentrifuged sample. For the uncentrifuged sample,

the NO_x⁻ concentration increased notably after 3 hours, whereas the centrifuged sample showed only a slight increase (fig. S5D). This suggests that the reduced particle density after centrifugation results from the loss of NBs through coalescence rather than the removal of suspended solids as these have no contribution in the NO_x⁻ formation. Together with our degassing experiments, these results strongly support that NBs are responsible for mediating the observed chemical activity.

We conducted an experiment in which pure H₂O₂ was added to a solution containing Fe²⁺, and the mixture was purged with air to generate bigger-sized bubbles. Our results show that NO_x⁻ production in this system is negligible compared to the NB experiments (fig. S6). This suggests that homogeneous bulk reactions between OH• and dissolved N₂ are extremely limited, and the GWI provided by NBs is essential for efficient NO_x⁻ formation. A small concentration of NO_x⁻ suggests that some reaction may occur either in the bulk or at the interface of larger millimeter-scale bubbles. However, such interfaces have significantly weaker electric fields, which likely limits the reaction rate. Hence, these contributions are minimal compared to the dominant interfacial chemistry occurring on NBs. Previously, it has been well established that GWI is crucial for the H₂O₂ generation (54). Thus, we can conclude that the gas-liquid interface of NBs is not only responsible for generating H₂O₂ but also

provide the crucial interfacial environment required for the oxidation of N_2 to NO_x^- .

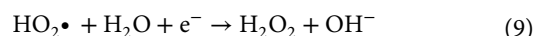
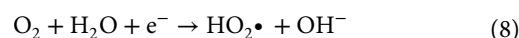
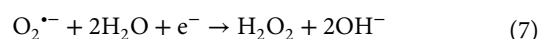
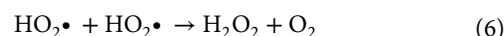
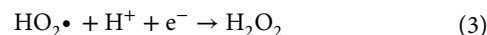
To verify whether reactive oxygen species (ROS) were generated from the gas line via triboelectric effects, a control experiment was performed by simply passing the gas through the line and bubbling it into water to generate large bubbles, without NB formation. If significant ROS such as $OH\cdot$ were produced due to contact electrification in the gas line, the resulting solution would exhibit detectable hydrogen H_2O_2 . Therefore, the amount of H_2O_2 formed in the nanobubbled solution was compared with that produced in the control (gas-bubbled) solution. The H_2O_2 concentration was quantified spectroscopically using ammonium molybdate $[(NH_4)_6Mo_7O_{24}]$ (55). A pronounced absorption peak at 353 nm was observed for the nanobubbled solution, whereas the control solution showed no significant signal (fig. S7A). This confirms that H_2O_2 and hence ROS such as $OH\cdot$ were generated in the nanobubbled system, with negligible contribution from triboelectric effects of the gas line. Furthermore, the presence of ROS in the nanobubbled system could result in nitrogen oxidation. Upon addition of a NO_x^- test reagent, the nanobubbled solution exhibited a brown coloration indicative of the NO_x^- formation, whereas the control solution showed no such color change (fig. S7B). These results collectively confirm that contact electrification from the gas line does not contribute appreciably to ROS generation, and that ROS formation originates primarily from NB activity.

To verify the source of nitrogen in the reaction, we carried out isotope-labeling experiments using $^{15}N_2$. When $^{14}N_2$ was introduced, the products displayed mass signals corresponding to $^{14}NO_3^-$ ($m/z = 62$) and $^{14}NO_2^-$ ($m/z = 46$). In contrast, replacement with $^{15}N_2$ resulted in the appearance of peaks at m/z 63 and 47, attributable to $^{15}NO_3^-$ and $^{15}NO_2^-$, respectively (fig. S8). These results clearly demonstrate that NO_x^- formation arises from the oxidation of N_2 within the NBs.

Spectrophotometric analysis provides the combined concentration of NO_2^- and NO_3^- (collectively referred to as NO_x^-) but does not provide the individual concentrations of NO_2^- and NO_3^- . Therefore, we used mass spectrometric quantification to determine the individual concentrations of NO_2^- and NO_3^- . However, it was also important to confirm that the NO_x^- concentration obtained from the mass spectrometric method and the spectrophotometric methods were consistent. As shown in fig. S9, the two methods exhibit excellent agreement, validating their reliability. This comparison ensures that NO_2^- and NO_3^- concentrations obtained from the mass spectrometric data were fairly accurate. To further support the accuracy of concentrations obtained by mass spectrometry, we additionally performed ion chromatography. The concentrations that are obtained by both these methods are in close agreement. The concentration distribution of NO_2^- and NO_3^- within the total NO_x^- yield calculated from mass spectrometry and ion chromatography is presented in fig. S10.

Figure 2C compares NO_x^- yields obtained when different feed gases, such as argon (Ar), N_2 , air, and an $O_2:N_2$ mixture (~1:1), were bubbled for 1 hour. A blank experiment with pure Ar (99.9%) produced only a trace amount of NO_x^- ($0.5 \mu M \text{ hour}^{-1}$), likely arising from residual dissolved air. In contrast, bubbling with compressed N_2 yielded a measurable amount of NO_x^- ($\sim 42 \mu M \text{ hour}^{-1}$). When N_2 was supplemented with O_2 in an approximate 1:1 ratio, productivity increased significantly to $\sim 56 \mu M$ after 1 hour. The highest NO_x^- yield ($\sim 61 \mu M \text{ hour}^{-1}$) was obtained using compressed air, demonstrating that air is a most effective feed gas for NO_x^- synthesis and highlighting

the feasibility of direct air utilization. The observed trend indicates that increasing O_2 in the feed gas enhances NO_x^- formation. This effect can be attributed, to the role of O_2 in generating H_2O_2 through perhydroxyl radical intermediate ($HO_2\cdot$) as follows (56–58)



The resulting H_2O_2 promotes $OH\cdot$ formation required for N_2 oxidation via reaction with Fe^{2+} . Although the $O_2:N_2$ (~1:1) mixture contains more O_2 than air ($O_2:N_2 \sim 1:4$), the NO_x^- yield is slightly lower, likely due to the reduced N_2 availability.

In our previous MB study (48), NO_3^- formation was more efficient under N_2 . This behavior can be attributed to the fact that, in MB systems, H_2O_2 is generated primarily through interfacial water/hydroxide oxidation ($OH^- \rightarrow OH\cdot \rightarrow H_2O_2$). Under N_2 , limited dissolved O_2 is available to scavenge radicals, allowing H_2O_2 to accumulate and drive Fenton-type oxidation toward NO_3^- . In contrast, the presence of O_2 in air introduces additional radical-scavenging pathways that reduce net H_2O_2 formation and consequently lower NO_x^- yields. In the present NB system, however, NO_x^- production is higher with air. Owing to their substantially larger interfacial area, stronger local electric fields, and longer lifetime, NBs facilitate efficient oxygen reduction ($O_2 \rightarrow O_2^{\bullet -} \rightarrow H_2O_2$) alongside water oxidation, making O_2 in the air a beneficial contributor to H_2O_2 generation. To support this conjecture, we measured H_2O_2 concentrations after 1 hour of micro- and nanobubbling under both N_2 and air. Microbubbling produced more H_2O_2 under N_2 than air, whereas nanobubbling showed the opposite trend, with air yielding higher H_2O_2 than N_2 (fig. S11), consistent with the proposed explanation.

To elucidate the dominant pathway of H_2O_2 formation in both MB and NB systems, isotopic labeling experiments were conducted using $^{18}O_2$ to trace the oxygen source in H_2O_2 . If the oxygen atoms in the detected H_2O_2 originate from O_2 , it indicates that interfacial oxygen reduction ($O_2 \rightarrow O_2^{\bullet -} \rightarrow H_2O_2$) is the predominant pathway; conversely, if they derive from water, it confirms water or hydroxide oxidation ($OH^- \rightarrow OH\cdot \rightarrow H_2O_2$) as the main route. 4-Carboxyphenyl boronic acid (100 μM) was used as a selective probe that reacts specifically with peroxides to yield the corresponding

phenol, incorporating the oxygen atom from the oxidant. In the MB system, mass spectrometric analysis of the reaction product revealed a peak at m/z 137.0237 (fig. S12A), corresponding to 4-hydroxybenzoic acid containing ^{16}O , indicating that H_2O_2 originates primarily from water oxidation. In contrast, the NB system exhibited dominant peaks at m/z 137.0241 and 139.0240 (fig. S12B), consistent with ^{16}O incorporation from water and ^{18}O incorporation from $^{18}\text{O}_2$, confirming that interfacial O_2 reduction along with water oxidation both contribute to the H_2O_2 generation under NB conditions.

As a control, air was directly purged into the aqueous Fe^{2+} solution, which produced only a trace amount of NO_x^- ($\sim 0.2 \mu\text{M hour}^{-1}$). This low yield can be attributed to the formation of larger bubbles during simple purging, resulting in limited gas-water interfacial area and curvature, which consequently reduced N_2 conversion. In contrast, introducing air through a microbubbler (MB size, 20 to 80 μm) led to a significantly higher NO_x^- yield ($\sim 16.9 \mu\text{M hour}^{-1}$). The highest productivity, however, was achieved when NBs were generated in the presence of Fe^{2+} , yielding $\sim 62.9 \mu\text{M hour}^{-1}$ (Fig. 2D). NBs have an exceptionally high surface area-to-volume ratio and strong interfacial curvature, enabling them to sustain enhanced electric fields that promote charge separation and radical generation at the gas-liquid interface. Their long lifetime in solution further allows reactive oxygen and nitrogen intermediates to accumulate and facilitates interfacial redox transformations to a greater extent. As a result, NBs produce significantly higher NO_x^- yields than MBs. In contrast, MBs, with their lower surface area-to-volume ratio, reduced interfacial curvature result in slightly weaker electric field as compared to NBs. Besides, shorter lifetime (faster collapse), offer shorter-lived reactive zones and less efficient radical coupling, leading to slower reaction rates and lower overall yields. When Fe^{2+} was absent, both MBs and NBs gave relatively low NO_x^- yields of $\sim 3.2 \mu\text{M hour}^{-1}$ and $\sim 9.3 \mu\text{M hour}^{-1}$, respectively. These results underscore the critical role of Fe^{2+} and NB interfacial chemistry in driving efficient NO_x^- production. When the NO_x^- testing reagent was introduced, a pronounced increase in the color intensity of the solution was observed for NB samples showing significantly stronger responses compared to MB or bulk solution (fig. S13).

To enable a fair comparison, we normalized the NO_x^- yields (μmol_p) from our NB system and the previously reported MB method (48) with respect to the gas-liquid interfacial area (m^2), the moles of gas supplied (mol_s), and the energy consumed (kWh). Upon comparison, the normalized NO_x^- yield obtained using NBs is $435.5 \mu\text{mol}_p \text{ m}^{-2} \text{ mol}_s^{-1} (\text{kWh})^{-1}$ (fig. S14), which is nearly five times higher than the normalized yield from MBs [$84.21 \mu\text{mol}_p \text{ m}^{-2} \text{ mol}_s^{-1} (\text{kWh})^{-1}$]. This demonstrates the superior efficiency of NBs in driving the reaction. We have also compared our NB-based result with previously reported MB system (48) as well as with electrocatalytic (15, 59–66) and photocatalytic processes (8, 67–70), where the yields are typically reported in $\mu\text{mol hour}^{-1} \text{ g}_{\text{cat}}^{-1}$ (fig. S15). This allows for a consistent and meaningful comparison across different methodologies. Figure S15 clearly shows that the NO_x^- yield obtained by using our NB method is significantly higher than that of the MB-generated method and almost all of the electro- and photocatalytic processes reported to date. This demonstrates the strong potential of our approach for scalable NO_x^- generation.

Electrostatic contributions to NB stability

One of the remarkable features of NBs is their exceptional stability, as they can persist in aqueous solutions for several days. Therefore,

we examined the long-term stability of air NBs in water. Figure 3A shows the NTA results demonstrating the stability of NBs when monitored at 24 and 72 hours following their generation. According to NTA measurements (fig. S16), the average NB size gradually increased from $136.6 \pm 3.6 \text{ nm}$ at the time of generation to $178.8 \pm 9.5 \text{ nm}$ after 24 hours, and further to $221.6 \pm 7.0 \text{ nm}$ after 72 hours. Over the same period, the NB concentration, denoted by C_{NB} , decreased from 2.11×10^8 bubbles/ml immediately after generation to 9.2×10^7 bubbles/ml at 24 hours and 7.0×10^7 bubbles/ml at 72 hours. The reduction in bubble count, coupled with the observed increase in size, can be attributed to random motion and collisions between NBs in the solution that promote coalescence and agglomeration over time. Although a gradual decline in concentration is evident, a substantial population of NBs persisted even after 72 hours. To check the stability of the generated NBs, we measured the laser light-scattering signal 14 days after nanobubbling. The scattering intensity remained clearly visible, indicating that NBs persist for at least 2 weeks (fig. S17). However, earlier studies have reported that NBs can remain stable for several months (71).

From the perspective of NO_x^- productivity, the stability of NBs plays a pivotal role, as prolonged bubble lifetime can enhance the reaction efficiency. To better exploit NB properties for improved yields, it is important to understand the factors that govern their stability. The most widely accepted explanation in the literature attributes NB stability to a balance between the Laplace pressure and electrostatic interactions at the NB-solvent interface (72). This relationship can be expressed through the Young-Laplace equation

$$P_0 + P_{\text{YL}} = P_{\text{NB}} + P_e \quad (10)$$

where P_0 is the external atmospheric pressure, P_{YL} is the Laplace pressure, P_{NB} is the pressure inside the NB, and P_e is the electrostatic pressure. If P_e is ignored, the calculated internal pressure of NBs becomes unrealistically high (73). For instance, substituting the surface tension of water ($\gamma = 0.072 \text{ N/m}$) and a NB radius of 100 nm into the Laplace relation,

$$P_{\text{YL}} = 2\gamma / r \quad (11)$$

gives $P_{\text{YL}} = 14.4 \text{ bar}$, which corresponds to an internal pressure of about 15.4 bar. Such high internal pressure would lead to rapid collapse unless additional stabilizing forces are present. This highlights the necessity of considering the electrostatic contribution (P_e), which counteracts surface tension and helps maintain NB stability.

Although Wang *et al.* (74) proposed that electrostatic interactions may be insufficient to fully counterbalance the Laplace pressure, Koshoridze and Levin (75) suggested that, from a theoretical standpoint, P_e could be large enough to significantly enhance NB stability. Motivated by these contrasting viewpoints, we investigated the role of electrostatic interactions between the NB and the surrounding environment. The factors that affect electrostatic interaction are (i) pH of the solution, (ii) gas inside the NBs, and (iii) nature of the dispersing solvent.

The influence of pH on NB size and concentration was systematically evaluated (Fig. 3B). Lower sizes and higher concentrations of NBs have been observed at neutral ($150 \pm 3.6 \text{ nm}$; 1.39×10^8 bubbles/ml) and basic pH ($135.6 \pm 3.5 \text{ nm}$; 2.04×10^8 bubbles/ml) values. This enhanced stability at higher pH can be attributed to the increased OH^- concentration, which strengthens the electrical double layer at the bubble interface and increases electrostatic repulsion, thereby suppressing agglomeration. In contrast, under acidic conditions

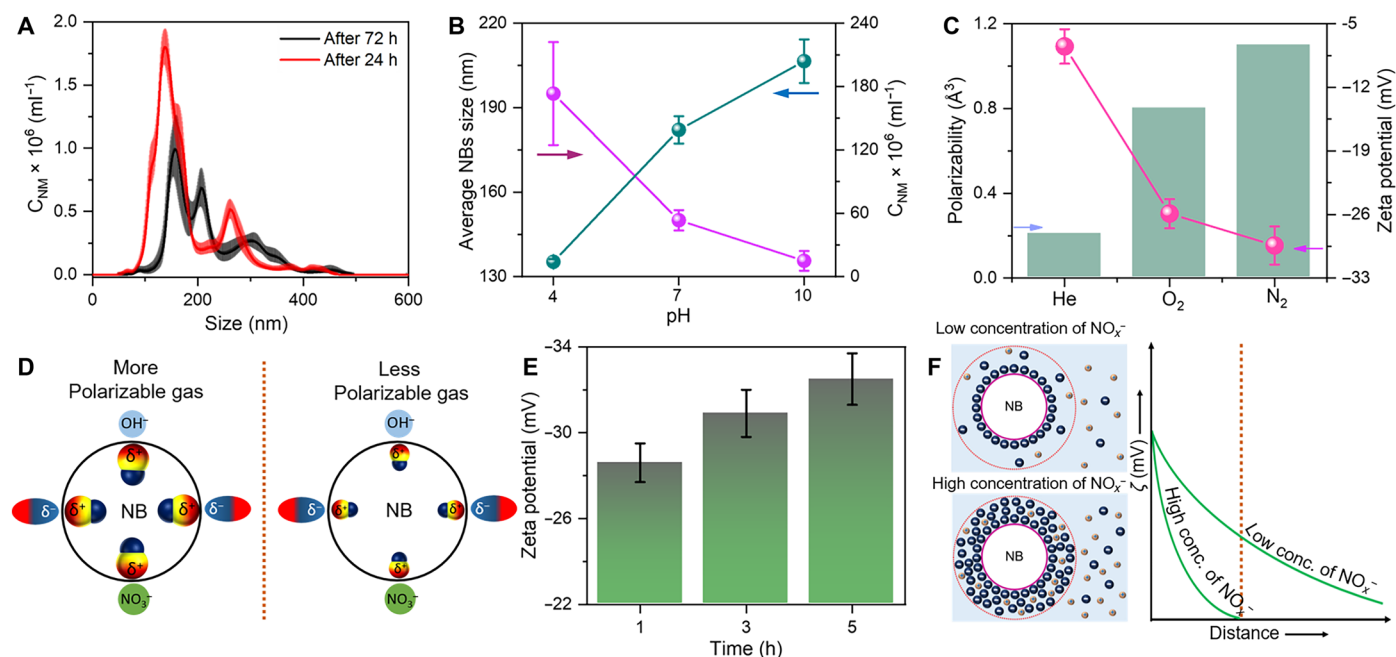


Fig. 3. Factors affecting NB stability in solution. (A) NTA measurements showing the stability of the NBs in the solution even after 24 and 72 hours (h) of their generation. (B) The effect of pH on the size and concentration of NBs. (C) The influence of polarizability of the gas present inside the NBs on the surface charges. (D) Schematic illustration of the gas polarizability effect on the surface charges. (E) The influence of bubbling time on zeta potential. (F) Schematic representation demonstrating the variation of surface charges on the NBs with different bubbling times.

(pH 4), the NB concentration decreased significantly (1.4×10^7 bubbles/ml) with a broader size distribution (150.8 ± 18.3 nm). The larger average size at low pH indicates reduced stability, likely due to diminished surface charge, which weakens electrostatic repulsion and promotes bubble coalescence.

According to the Derjaguin-Landau-Verwey-Overbeek theory of colloidal stability, the extent of surface charge expressed as the zeta potential plays a central role in determining the stability of monodisperse colloidal systems (76, 77). In NB suspensions, interactions with surrounding species such as solvents, OH⁻, or NO_x⁻ generated during the reaction can induce dipoles on the bubble surface through dipole-dipole or ion-dipole mechanisms. The resulting zeta potential, and hence the stability of the NBs, depends on how effectively the bubble surface accommodates these induced dipoles. This ability is closely related to the polarizability (α) of the gas molecules or atoms, which describes how readily their electron cloud can be distorted by an external electric field. A higher polarizability indicates a greater capacity of the gas phase to adjust its electron density and, in turn, to sustain surface charge at the NB interface. We investigated the zeta potentials of NBs formed from gases with varying polarizabilities. A clear correlation emerged between the measured zeta potential and the polarizability of the gas (Fig. 3C). Among the systems studied, helium (He)-loaded NBs displayed the least negative potential ($\zeta_{\text{He}} = -7.5 \pm 1.9$ mV). The ζ_{O_2} is measured to be -25.9 ± 1.6 mV, which is less negative than the ζ_{N_2} (-29.4 ± 2.1 mV). The zeta potential values followed the order $\zeta_{\text{He}} < \zeta_{\text{O}_2} < \zeta_{\text{N}_2}$, which corroborates the order of the atomic or molecular polarizabilities in these gases: α_{He} (0.208 \AA^3) $<$ α_{O_2} (0.802 \AA^3) $<$ α_{N_2} (1.1 \AA^3). These findings strongly support our hypothesis that NB stability is governed by the polarizability of the gas inside the NBs. A conceptual illustration of this stabilization

mechanism is presented in Fig. 3D. The nature of the solvents used is also likely to influence electrostatic interactions. However, for the present study on NO_x⁻ generation, this factor is not relevant because water was exclusively used as the solvent. Consequently, the effect of different solvents on NB stabilization was not investigated.

The influence of bubbling time on the zeta potential was also examined. A progressive increase in surface charge was observed with longer bubbling durations. After 1 hour of nanobubbling, the zeta potential was -28.6 ± 0.9 mV, which further increased to -30.9 ± 1.1 mV at 3 hours and -32.9 ± 1.2 mV at 5 hours (Fig. 3E). This trend indicates that extended bubbling enhances the accumulation of negatively charged NO_x⁻ species at the bubble interface, thereby increasing the net negative surface charge. A schematic representation of this process is shown in Fig. 3F. The resulting increase in surface charge density promotes stronger electrostatic repulsion between bubbles, leading to improved NB stability.

As the stability of the NBs is ensured by the electrostatic interaction, we also checked the effect of ionic strength on the stability and activity of NBs. We found that the addition of electrolytes significantly influences NB stability. Increasing ionic strength (salt concentration) compresses the electric double layer and reduces the zeta potential of the NB surface, thereby weakening electrostatic repulsion. As a result, NBs approach each other more easily and undergo faster coalescence. This leads to the formation of larger, less stable bubbles, and a reduction in the population of stable NBs ultimately leads to lower yield, as shown in fig. S18A. We also examined the influence of monovalent (Na⁺ and K⁺) and divalent (Ca²⁺) chloride salts on NO_x⁻ production. The concentration of each salt was kept constant (0.1 mM). Among the monovalent ions, Na⁺, being smaller and having a higher polarizing power than K⁺, more effectively perturbs the electrostatic stability of NBs. This leads to faster coalescence

and, consequently, a lower NO_x^- yield compared to K^+ . The divalent ion, Ca^{2+} , produces much stronger charge screening at the bubble interface as compared to Na^+ or K^+ , causing rapid coalescence and a marked reduction in the population of stable NBs. This pronounced destabilization is directly reflected in the significantly lower NO_x^- yield observed in the presence of Ca^{2+} (fig. S18B).

Influence of reaction parameters on NB-mediated NO_x^- generation

When the pH of the initial solution was adjusted from acidic to basic, the formation of NO_x^- increased significantly (fig. S19). This behavior arises from the increased availability of OH^- ions at higher pH. An increase in OH^- enhances the generation of H_2O_2 within NBs. This, in turn, promotes the Fenton reaction to produce more $\text{OH}\cdot$ and to boost NO_x^- yield. In addition, excess OH^- at the interface stabilizes NBs through electrostatic repulsion of negatively charged species, as discussed previously in Fig. 3B. Enhanced NB stability provides a larger interfacial surface area, facilitating higher NO_x^- production. In contrast, at lower pH values, NBs are less stable and prone to coalescence into larger bubbles with reduced surface area, ultimately leading to lower yields.

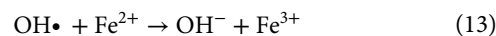
As noted in Eq. 5, one pathway for H_2O_2 generation involves the recombination of two $\text{HO}_2\cdot$. While $\text{HO}_2\cdot$ has a low pK_a (~4.8) and is expected to deprotonate to $\text{O}_2^{\cdot-}$ at higher pH, potentially reducing H_2O_2 formation. However, we observe the opposite trend where NO_x^- production increases under alkaline conditions (fig. S19), indicating higher H_2O_2 levels. This apparent contradiction can be rationalized as follows. First, Eq. 5 describes an equilibrium process, and complete conversion of $\text{HO}_2\cdot$ to $\text{O}_2^{\cdot-}$ does not occur. A small but finite population of $\text{HO}_2\cdot$ can persist even at high pH, especially at the GWI where local electric fields, solvation environments, and proton activity differ markedly from the bulk solution. Second, the role of O_2 is to facilitate the H_2O_2 formation during N_2 oxidation. It is well established that water alone at a hydrophobic interface can produce H_2O_2 even without external O_2 input (17). At lower pH, O_2 promotes H_2O_2 generation through $\text{HO}_2\cdot$ formation. At higher pH, however, the dominant contribution shifts and the higher concentration of OH^- enhances interfacial oxidation ($\text{OH}^- \rightarrow \text{OH}\cdot + \text{e}^-$), followed by radical recombination ($2\text{OH}\cdot \rightarrow \text{H}_2\text{O}_2$), despite the favored deprotonation of $\text{HO}_2\cdot$ to $\text{O}_2^{\cdot-}$. As a result, H_2O_2 production increases at elevated pH, which is reflected in the NO_x^- yields, as shown in fig. S19.

One might expect Fe^{2+} and Fe^{3+} to precipitate as hydroxides at elevated pH, as commonly observed in classical Fenton chemistry. However, in our system, increasing the pH enhances the local OH^- concentration at the NB interface, which in turn promotes interfacial oxidation ($\text{OH}^- \rightarrow \text{OH}\cdot + \text{e}^-$) followed by radical recombination ($2\text{OH}\cdot \rightarrow \text{H}_2\text{O}_2$). This interfacial pathway dominates over the precipitation of $\text{Fe}^{2+}/\text{Fe}^{3+}$ hydroxides typically observed in classical Fenton chemistry. Consistent with this, no visible precipitation or turbidity was observed at high pH. To further verify the absence of Fe precipitation, inductively coupled plasma–mass spectrometry (ICP-MS) analysis of the Fe^{2+} solution immediately after nanobubbling at pH 9 showed no measurable loss of Fe, with concentrations matching the initial Fe^{2+} level. The unchanged Fe^{2+} concentration also supports the catalytic role of Fe^{2+} in the reaction, with any Fe^{3+} formed being rapidly reduced back to Fe^{2+} via the following reaction (15)



Moreover, continuous pH monitoring revealed a gradual decrease in pH over time, indicating increasing acidity from H^+ generation. This trend aligns with our previous observation (48) and is attributed to the formation of H^+ as counterions to the accumulating NO_x^- species, thereby allowing Fe^{2+} to remain soluble in water. The time-dependent evolution of pH is shown in fig. S20.

The influence of Fe^{2+} concentration on NO_x^- formation was also evaluated. As shown in fig. S21, NO_x^- yield initially increased with Fe^{2+} concentration and then declined at higher concentrations. This trend can be explained by interfacial processes. At moderate levels, the presence of more Fe^{2+} ions at the bubble-liquid interface enhances Fenton's reaction and facilitates N_2 activation, thereby boosting NO_x^- production. Once the interfacial sites become saturated, excess Fe^{2+} migrates into the bulk solution, where they do not participate in H_2O_2 generation or N_2 activation. Instead, they consume $\text{OH}\cdot$ via the competing reaction (78)



This radical scavenging lowers the $\text{OH}\cdot$ concentration available for N_2 activation, ultimately reducing the efficiency of NO_x^- generation.

In the earlier time-dependent experiments (Fig. 2B), enhanced NO_x^- production was observed upon continuous nanobubbling. Given that NBs remain stable for several days, we next investigated whether NO_x^- could be produced in the absence of continuous bubbling. Air was bubbled for 1 hour, yielding an initial NO_x^- concentration of $58.3 \pm 6.9 \mu\text{M}$. After bubbling was stopped, the concentration increased to $73 \pm 10.1 \mu\text{M}$ at 6 hours and reached a plateau of $75 \pm 5.2 \mu\text{M}$ at 12 hours (fig. S22). These results indicate that pre-existing NBs continue to drive NO_x^- formation, but only to a limited extent before saturating. This behavior is likely due to gradual NB coalescence into larger bubbles, which eventually evolve into MBs that rise and release gas, thereby reducing both NB abundance and the gas content available for reactions. This interpretation is supported by fig. S16, which shows a decline in NB concentration over time due to coalescence. On the other hand, continuous bubbling maintains a steady supply of NBs. Although coalescence still occurs, the persistent generation ensures a sufficient NB population, leading to a sustained increase in NO_x^- concentration.

When nanobubbling is active, the bubble surfaces are constantly being renewed. This creates a fresh, highly reactive interface that continuously forms short-lived oxidants (such as $\text{OH}\cdot$ and H_2O_2) and maintains strong local chemical gradients. These are the conditions that drive fast NO_x^- formation. Once nanobubbling stops, this reactive, nonequilibrium interface quickly disappears. The radicals and other reactive species decay within minutes to hours, and the bubble surfaces become aged and much less active. Even though the total surface area stays nearly the same, the reactivity per unit area becomes much lower, which could be the reason for the sharp decrease in NO_x^- production postbubbling.

Another factor that may contribute to the sharp decrease in NO_x^- production after stopping nanobubbling is the accumulation of negatively charged species on the bubble surfaces. NBs are stabilized by a negatively charged interface, and during NO_x^- formation, this negative charge increases further as more NO_x^- ions are produced and adsorb onto the surface. Over time, this buildup of surface-bound anions can block or passivate the reactive sites on the bubbles. As a result, the effective reactive surface area becomes significantly smaller, even though the geometric surface area of the bubbles remains nearly unchanged. This surface passivation lowers the interfacial reactivity

and further explains the strong decline in NO_x^- production once active bubbling stops. A further factor could be the faster diffusion of NBs during continuous bubbling. Active nanobubbling not only generates new bubbles but also keeps the existing ones moving rapidly through the solution due to the upward gas flow. This fast movement allows NBs to continuously encounter fresh regions of the liquid, increasing their exposure to new interfacial environments where ROS can be generated. In contrast, once bubbling stops, NB motion becomes diffusion-limited and much slower. With reduced movement, NBs interact with far fewer fresh interfacial regions, which significantly lowers the formation of ROS and therefore reduces NO_x^- production.

Catalytic activity of Fe^{2+}

We propose that Fe^{2+} functions as a catalyst during the NB-assisted conversion process. The Fe^{3+} formed in the reaction can be electrochemically reduced to Fe^{2+} at the interface by the pathway shown in Eq. 12 (15).

To verify whether the regeneration of Fe^{2+} indeed proceeds via the formation of HO_2^\bullet as described in Eq. 12, we carried out radical-trapping experiments using 2,2,6,6-tetramethylpiperidin-1-yl oxyl (TEMPO) as a spin trap. For this study, N_2 was supplied as the nitrogen source instead of air. Because dissolved O_2 in air could independently generate HO_2^\bullet within NBs (as shown in Eq. 8), its presence would interfere with the HO_2^\bullet signals generated from the catalytic regeneration of Fe^{2+} . The resulting mass spectrum was presented in fig. S23. Characteristic peaks at m/z 157.1472 (TEMPO-H) and m/z 158.1466 (TEMPO-H-H) confirm the presence of H^\bullet , while a signal at m/z 174.1488 (TEMPO-H-OH) indicates OH^\bullet generated via the Fenton pathway. Notably, a distinct peak at m/z 190.1448 corresponding to

TEMPO-H-OOH was observed, providing clear evidence for the presence of HO_2^\bullet . These results demonstrate that HO_2^\bullet is formed during the process, supporting our proposed pathway as shown in Eq. 12 to regenerate Fe^{2+} , thereby sustaining catalytic activity in the system.

Mechanistic insights into air-to- NO_x^- conversion

To elucidate the mechanism of air-to- NO_x^- conversion, it is crucial to identify reaction intermediates formed during the process, as they provide insights into the underlying pathway. The intermediates were detected using ex situ attenuated total reflection Fourier transform infrared spectroscopy (ATR-FTIR). While in situ FTIR is typically required due to the short-lived nature of such intermediates, the remarkable stability of NBs in solution enables ex situ ATR-FTIR analysis. Because NBs remain stable over extended periods, reactions continue to occur at the NB interface, allowing continuous generation and subsequent detection of intermediates. ATR-FTIR spectra of the NB samples recorded immediately after different bubbling times is presented in Fig. 4A. The infrared absorption spectra exhibited a broad peak centered at 1050 cm^{-1} , confirming the presence of NO generated during the reaction (79). A characteristic vibrational bands assigned to $\text{H}_2\text{N}_2\text{O}_2$ was observed at $\sim 1232\text{ cm}^{-1}$ (15). The $\text{H}_2\text{N}_2\text{O}_2$ band at $\sim 1232\text{ cm}^{-1}$ exhibited intensity fluctuations at different times. For instance, the $\text{H}_2\text{N}_2\text{O}_2$ peak appeared in samples collected after 2, 3, and 5 hours of nanobubbling, but was absent in the 1 and 4 hours samples. These observations indicate that $\text{H}_2\text{N}_2\text{O}_2$ serves as an intermediate that is continuously formed and subsequently converted into NO_2^- and NO_3^- . In contrast, the signals corresponding to NO_3^- (1330 to 1400 cm^{-1}) and NO_2^- (1260 to 1300 cm^{-1}) increased steadily, as these are the stable species

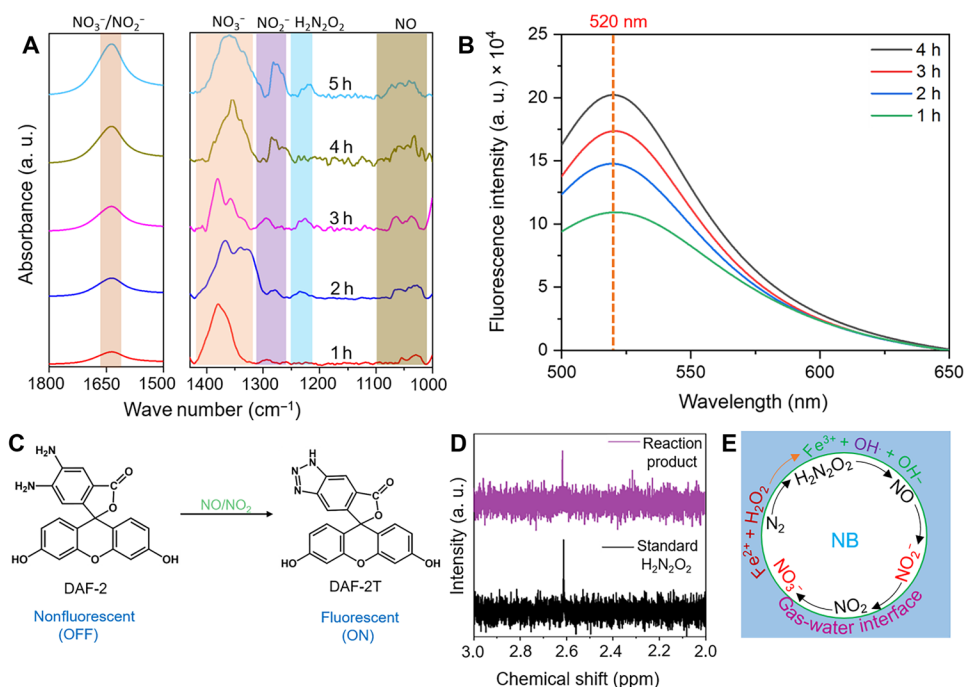
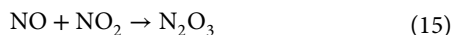
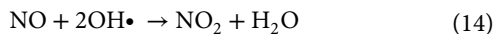


Fig. 4. Mechanistic understanding of NO_x^- formation. (A) Time-dependent ex situ ATR-FTIR characterization of the nanobubbled solution. (B) Time-dependent variation in the fluorescence intensity of the DAF-2T solution during air bubbling. (C) Schematic illustration of the transformation of nonfluorescent DAF-2 into fluorescent DAF-2T upon reaction with NO/NO_2 in the medium. (D) A Comparison of the ^1H -NMR spectrum of the reaction product obtained after 1 hour of nanobubbling and the standard $\text{H}_2\text{N}_2\text{O}_2$ solution. (E) Schematic representation of the plausible pathway for the conversion of N_2 to $\text{NO}_2^-/\text{NO}_3^-$ at the air-water interface of NBs.

and final products of the transformation (80, 81). In addition, a vibrational band at $\sim 1650\text{ cm}^{-1}$ also arises corresponding to either NO_2 or $\text{H}_2\text{N}_2\text{O}_2$ feature or a combination of both (15). ATR-FTIR spectra confirms the existence of $\text{H}_2\text{N}_2\text{O}_2$, NO, and NO_2 as the possible intermediates along with the final products (NO_2^- and NO_3^-).

To further confirm the presence of NO and NO_2 in the solution, diamino fluorescein (DAF-2) was used as a fluorescence indicator. DAF-2 is only weakly fluorescent, but in the presence of NO and $\text{OH}\cdot$ it undergoes a chemical transformation to generate a highly fluorescent triazole derivative, known as DAF-2T. The transformation is thought to proceed through the intermediate formation of nitrous anhydride (N_2O_3), produced via the following steps



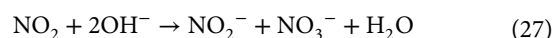
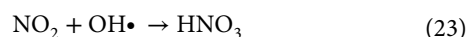
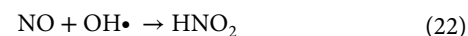
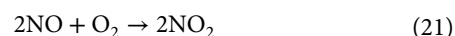
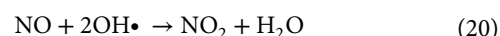
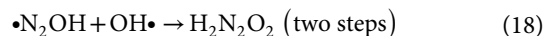
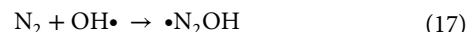
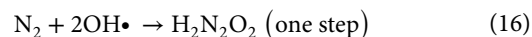
The in situ–formed N_2O_3 subsequently reacts with the vicinal diamine groups of DAF-2 to produce the fluorescent DAF-2T.

A 5 mM solution of DAF-2 in dimethyl sulfoxide was introduced into the nanobubbled solution. With increasing air-bubbling time, a progressive rise in fluorescence intensity ($\lambda_{\text{ex}} = 485\text{ nm}$ and $\lambda_{\text{em}} = 520\text{ nm}$) was observed (Fig. 4B). Notably, while free DAF-2 exhibits only weak fluorescence, a substantial enhancement was recorded after 4 hours of bubbling (fig. S24). This fluorescence amplification indicates an accumulation of N_2O_3 in solution, which reacts with DAF-2 to yield DAF-2T (Fig. 4C) (82). To confirm that the enhanced fluorescence signal of DAF-2T originates specifically from NO/ NO_2 generated in the system and not from false positives, we performed control experiments using 2-(4-carboxyphenyl)-4,4,5,5-tetramethylimidazole-1-oxyl-3-oxide (cPTIO), a well-known NO scavenger. Upon addition of 100 μM cPTIO to the reaction system, the fluorescence intensity of DAF-2T was almost completely quenched compared to the control sample without cPTIO (fig. S25). This suppression of fluorescence clearly indicates that the observed DAF-2T signal arises from NO formation, as cPTIO effectively scavenges NO, thereby preventing its reaction with DAF-2 to produce the fluorescent DAF-2T species. We further performed $\text{OH}\cdot$ scavenging experiments using isopropanol (IPA) to verify the role of $\text{OH}\cdot$ in NO/ NO_2 generation. Upon addition of 10% (v/v) IPA to the reaction mixture, the fluorescence intensity of DAF-2T markedly decreased compared to the control without IPA (fig. S26A). Since IPA efficiently quenches $\text{OH}\cdot$ radicals formed during the Fenton reaction, this suppression of fluorescence indicates that $\text{OH}\cdot$ plays a crucial role in initiating NO/ NO_2 formation, which subsequently reacts with DAF-2 to produce the fluorescent DAF-2T species. Moreover, the addition of IPA also significantly reduced the overall NO_x^- yield (fig. S26B), further confirming the essential role of $\text{OH}\cdot$ radicals in the N_2 oxidation pathway. These results confirm that both NO and NO_2 are indeed generated at the NB interface during the reaction.

Additional confirmation was obtained through 5,5-dimethyl-1-pyrroline-*N*-oxide (DMPO) spin-trapping experiments, in which NO and NO_2 were detected as DMPO adducts at m/z 143.0856 (DMPO-NO) and m/z 159.0848 (DMPO- NO_2), respectively (fig. S27). We performed $^{15}\text{N}_2$ isotope-labeling spin-trapping experiments to further verify the formation of NO and NO_2 radical intermediates in our system. When the reaction was carried out using $^{15}\text{N}_2$ as the feed gas in the presence of DMPO, the resulting mass spectra revealed distinct signals corresponding to DMPO- ^{15}NO and DMPO- $^{15}\text{NO}_2$

adducts at m/z 144.0864 and m/z 160.0856, respectively (fig. S28). The observation of these ^{15}N -labeled adducts provides direct evidence that both NO and NO_2 radicals are generated during the reaction process. Complementary ^1H nuclear magnetic resonance (NMR) measurements were performed to corroborate the infrared identification of $\text{H}_2\text{N}_2\text{O}_2$. The nanobubbled sample showed a distinct signal at 2.6 parts per million (Fig. 4D), consistent with $\text{H}_2\text{N}_2\text{O}_2$ (15). The presence of $\text{H}_2\text{N}_2\text{O}_2$ was further validated by recording the spectrum of a standard $\text{H}_2\text{N}_2\text{O}_2$ solution, which displayed a peak with an identical chemical shift.

On the basis of all the above spectroscopic evidence, we propose that $\text{OH}\cdot$ first activates N_2 molecules to generate the intermediate $\text{H}_2\text{N}_2\text{O}_2$ (Eqs. 16 to 18). This species subsequently decomposes to produce NO in the presence of $\text{OH}\cdot$ (Eq. 19). The NO formed is then oxidized to NO_2 by $\text{OH}\cdot$ and O_2 (Eqs. 20 and 21). Further transformations occur via additional oxidation of NO and NO_2 by $\text{OH}\cdot$ (Eqs. 22 and 23) and through redox reactions involving $\text{OH}\cdot$ and OH^- (Eqs. 24 to 27), ultimately yielding NO_3^- and NO_2^- as the final products (Fig. 4E). Typically, NB reactions occur at the GWI, which takes place within a few Debye lengths away (vicinity of the interface) from the boundary on the few nanoseconds to microseconds timescale. Therefore, we believe that the sequential steps (16–27) also occur near the interface within this timeframe



We acknowledge that the formation of NO_x^- may not be limited to the pathway described here, and additional intermediates or mechanisms that we were unable to detect could also contribute. Nevertheless, our experimental observations strongly support the pathways we have proposed as being active under the studied conditions.

One of the key aspects of this NB work is the consumption of lower energy compared to other methods. Therefore, we made a rough estimate of the NO_x^- yield per gram per hour per kWh of energy consumption, incorporating a breakdown of the energy inputs associated with compression, vibration, and other system components. Our calculation shows that the NB system delivers approximately $54.93 \text{ mol hour}^{-1} \text{ g}^{-1} \text{ kW hour}^{-1}$ (fig. S29), outperforming the industrial route (Haber-Bosch + Ostwald) as well as MB-based, electrochemical, and photocatalytic methods. This markedly higher value arises from the substantially lower energy demand of the NB process, highlighting its superior energy efficiency and potential for scalable implementation.

DISCUSSION

NO_3^- is a key inorganic nitrogen source that supports plant growth and productivity (1). Plants can acquire nitrogen from the soil primarily as ammonium (NH_4^+) or NO_3^- , but many crops preferentially take up NO_3^- because their roots possess both high and low-affinity NO_3^- transport systems. These operate effectively across a broad concentration range from micromolar to millimolar, allowing plants to absorb NO_3^- even under low external availability (83, 84). In several production systems such as hydroponics and aquatic biomass cultivation, external NO_3^- concentrations in the tens of micromolar range are already sufficient to support growth or alleviate nitrogen limitation (85, 86). For instance, concentrations of $10 \mu\text{M}$ can sustain seedling development or maintain growth in nitrogen-sensitive crops, highlighting that biologically meaningful uptake occurs at this level (86). Our NB-based approach reliably generates $\sim 60 \mu\text{M}$ NO_x^- within 1 hour, increasing to $\sim 294 \mu\text{M}$ after 5 hours of bubbling. A key advantage of this method is that nitrate concentration can be tuned through continuous bubbling, enabling tailored nutrient delivery according to the requirements of different crops. Such flexibility makes it particularly well-suited for on-site fertilizer production.

From an agronomic and deployment point of view, producing NO_3^- on site and delivering it via irrigation (fertigation) has several benefits over centralized fertilizer manufacture and shipment. NO_3^- is mobile in the root zone and is immediately available for plant uptake, which simplifies integration with drip or micro-irrigation systems and reduces the need for on-farm chemical transformation (e.g., nitrification of NH_4^+) (87). Because NO_3^- is typically less phytotoxic than high concentrations of free NH_4^+ for many species. On-demand nitrate supply reduces the risk of acute ammonium toxicity that can occur if NH_4^+ concentrations spike in the irrigation water (88).

From a deployment perspective, our strategy (Fig. 5) envisions large tanks where portable nanobubblers will continuously enrich water with NO_3^- . The NO_3^- -enriched water can then be supplied directly through irrigation channels, functioning simultaneously as both irrigation and fertilizer solution. The nitrogen source (air) is free, oxygen is derived from air or water, and the energy requirements for air suction and nanobubbler operation can be met using renewable sources such as solar power.

On-site generation of micromolar NO_3^- is already agronomically useful in two contexts: (i) as a continuous, low-level nutrient feed for seedlings, hydroponic systems, and specialty crops requiring modest nitrogen inputs; and (ii) as a supplemental fertigation source that reduces reliance on bulk fertilizer deliveries while lowering transport-related CO_2 emissions. Together, these agronomic and sustainability benefits establish in situ NO_3^- generation, even at micromolar concentrations, as a defensible strategy for decentralized, low-carbon fertilization. By enabling tailored, on-demand delivery, our method will offer a pathway toward reducing dependence on energy-intensive Haber-Bosch nitrogen fixation while meeting the nutrient demands of modern agriculture.

To evaluate the environmental safety of NO_x^- -enriched water, particularly with respect to potential phytotoxicity associated with NO_2^- and Fe^{2+} , we assessed the concentrations generated under typical operating conditions. This is important because uncontrolled discharge or direct agricultural use without proper management could pose risks to plants and soil-microbial systems. In our system, the total NO_x^- concentration typically remains below 20 to 30 mg liter^{-1} , with NO_2^- contributing $< 10 \text{ mg liter}^{-1}$, well below the

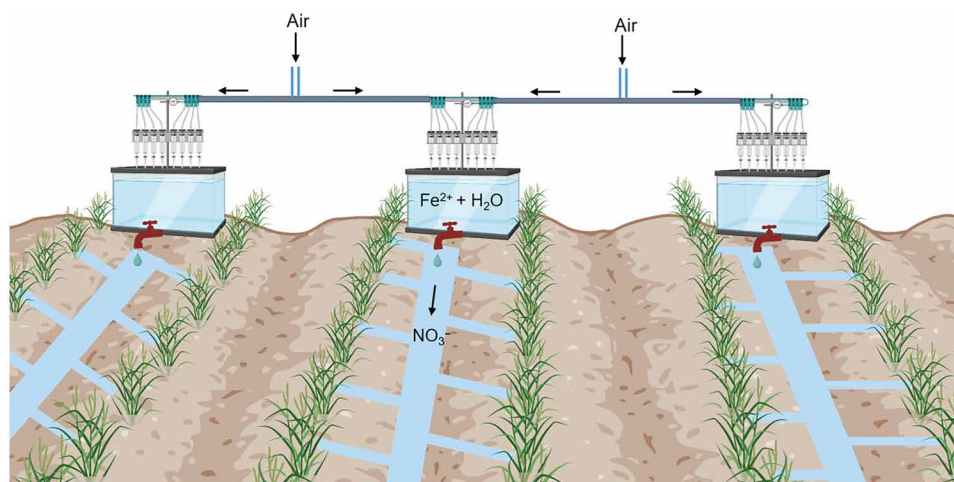


Fig. 5. Schematic of the proposed multi-nanobubbler device for on-site generation of NO_3^- as a liquid fertilizer and delivery to plants via irrigation channels.

phytotoxic threshold (~ 50 mg liter $^{-1}$). Moreover, prolonged nanobubbling or operation under oxygen-rich conditions gradually converts NO_2^- to the more stable and plant-available NO_3^- , inherently minimizing the accumulation of NO_2^- . The use of nitrifying bacteria such as *Nitrosomonas* and *Nitrobacter* in controlled biofilters or soil environments can naturally oxidize NO_2^- to NO_3^- , offering a sustainable, biological route for effluent refinement. The Fe^{2+} concentration in the treated solution (~ 50 μM) can be efficiently reduced by mild aeration or filtration through natural zeolites, clays, or Fe-chelating agents. As a result, the final effluent composed of NO_3^- aligns with standard nitrate-based fertilizers, and low Fe levels (after post-treatment) can serve as beneficial micronutrients without posing ecological risks.

NBs have been used in agriculture and water treatment for many years, and their effects on plant growth arise from a broad combination of physicochemical processes, not only from NO_x^- generation. GWIs are known to host a wide variety of interfacial reactions, including the formation of ROS, whose impact on soil and plant systems can vary widely and may sometimes be detrimental. Therefore, the chemistry demonstrated in this work should not be considered directly translatable to agricultural practice at this stage. Moreover, the Fe^{2+} concentration used in our experiments (50 μM) does not reflect typical soil conditions, although we believe that Fe^{2+} concentration can be reduced by mild aeration or filtration through natural zeolites, clays, or Fe-chelating agents, but it has yet to be tested. At the current stage, any potential relevance of this chemistry to plant or soil systems is based on our vision and would require substantial interdisciplinary evaluation, including plant biology, soil chemistry, environmental safety, and long-term field studies. The key contribution of this work is fundamental, which demonstrates that NB interfaces can mediate the oxidation of N_2 to NO_x^- and reveals the mechanistic importance of the gas-liquid interface in enabling such chemistry. Nevertheless, we have added to the supporting information a comparison with other ways of generating NO_x^- and a discussion of energy consumption compared to other techniques. Both comparisons suggest that the NB generation method holds much promise.

In summary, we present a simple, energy-efficient, and scalable strategy for converting atmospheric N_2 into NO_3^- and NO_2^- using NBs at the GWI. Air NBs generated with a vibrating porous carbon fiber device in the presence of Fe^{2+} facilitate Fenton's reaction, producing $\text{OH}\cdot$ that activates N_2 without external potential or radiation. Compared to MBs, NBs provide greater interfacial area and curvature, which results in enhanced electric fields and yields a fourfold increase in NO_x^- production (~ 60 μM hour $^{-1}$). Mechanistic studies confirm intermediates such as $\text{H}_2\text{N}_2\text{O}_2$, NO , and NO_2 drive stepwise conversion to NO_x^- . NB stability, governed by factors affecting electrostatic interactions, enables sustained reactions. This approach allows tunable, on-site NO_3^- generation at concentration levels suitable for fertigation and hydroponics, offering a green alternative to centralized, energy-intensive nitrogen fixation. NB-mediated air-to- NO_x^- conversion will provide a practical platform for sustainable, low-carbon agricultural nitrogen management.

MATERIALS AND METHODS

Reagents and materials

Ferrous sulfate heptahydrate ($\text{FeSO}_4 \cdot 7\text{H}_2\text{O}$), sodium nitrate (NaNO_3), sodium nitrite (NaNO_2), hydrochloric acid (HCl), sodium hydroxide (NaOH), and PTO were all purchased from Thermo Fisher Scientific.

TEMPO, DMPO, sulfanilamide ($\text{C}_6\text{H}_8\text{N}_2\text{O}_2\text{S}$), and *N*-(1-naphthyl) ethylenediamine dihydrochloride (NEDA) were obtained from Sigma Aldrich. Ultrahigh pure compressed air (99.99%), dinitrogen (N_2 , 99.99%), oxygen (O_2 , 99.99%), and argon (Ar , 99.99%) were acquired from Praxair Inc. The isotope-labeled N_2 gas ($^{15}\text{N}_2$, 98%) and deuterium oxide (D_2O , 98%) were ordered from Cambridge Isotope Laboratories. High-performance liquid chromatography (HPLC)-grade water purchased from Merck was used in the NB experiments. All the chemicals were used as purchased without any purification.

Sample preparation for NB-related studies

Air NBs were generated using a custom-built NB generator that introduces gas into water through a carbon fiber membrane at 30 psi under controlled conditions. For pH variation studies, aqueous solutions were adjusted to pH 4 and pH 10 using dilute HCl and NaOH , respectively, and confirmed with a calibrated benchtop pH meter (± 0.01 accuracy). NB samples were freshly prepared before each measurement. For pH stability analysis, air NBs were generated in water at pH 7, and the size and concentration were monitored immediately after generation, and subsequently at 24- and 72-hour intervals. Additional measurements were performed on freshly prepared NB samples at pH 4 and pH 10.

$^1\text{H-NMR}$ for the detection of $\text{H}_2\text{N}_2\text{O}_2$

Nanobubbling was carried out for 1 hour, and the resulting sample was analyzed by NMR within 5 min to minimize the loss of $\text{H}_2\text{N}_2\text{O}_2$ due to its rapid decomposition. For each measurement, 630 μl of the nanobubbled solution was mixed with 70 μl of D_2O . D_2O was used to lock the NMR signal. Water-suppressed $^1\text{H-NMR}$ spectra were collected with 32 scans on a Varian Inova 600-MHz spectrometer equipped with a z-gradient triple-resonance hydrogen-carbon-nitrogen (HCN) probe. The spectral data were processed in MestReNova, including manual phasing and baseline correction with the Whittaker Smoother algorithm. The observed chemical shift was validated against a reference spectrum obtained from a standard $\text{H}_2\text{N}_2\text{O}_2$ solution.

ATR-FTIR analysis

Infrared spectra of the NB-containing samples were acquired on a Nicolet iS50 FTIR spectrometer equipped with a diamond ATR accessory. Data were collected in the range of 4000 to 400 cm^{-1} using a DLaTGS-KBr detector, with a spectral resolution of 4 cm^{-1} and an average of 32 scans per spectrum.

Fluorescence measurement

Fluorescence study of the sample was conducted using Horiba FluoroLog-3 fluorimeter equipped with 450 W Xenon lamp as a light source and detected using a photomultiplier tube (PMT) detector in the range 500 to 700 nm.

Quantification of H_2O_2 using PTO

PTO was used as a reagent for the colorimetric determination of H_2O_2 . Equal volumes of 0.1 M PTO solution and the sample were mixed and allowed to react for 15 min. The resulting solution exhibited a characteristic absorbance at 400 nm, which was recorded using an ultraviolet-visible (UV-vis) spectrophotometer. For quantitative analysis of H_2O_2 , a calibration curve was generated with standard H_2O_2 solutions.

Identification of H₂O₂ using ammonium molybdate

In brief, 20 μ l each of solution A [0.4 M KI, 0.1 M NaOH, and 0.02 mM ammonium molybdate, (NH₄)₆Mo₇O₂₄] and solution B (0.1 M potassium hydrogen phthalate) were mixed with 20 μ l of either the nanobubbled or control solution. The mixtures were analyzed using a UV-vis spectrophotometer at 353 nm, corresponding to the absorption of triiodide (I₃⁻), which forms from the oxidation of iodide (I⁻) in the presence of H₂O₂ catalyzed by (NH₄)₆Mo₇O₂₄.

Spectrophotometric quantification of NO_x⁻

NO_x⁻ (NO₂⁻/NO₃⁻) concentration in the solution was analyzed spectrophotometrically through the diazotization reaction of sulfanilamide. A sulfanilamide reagent was prepared by dissolving 1% (w/v) sulfanilamide in 1% (v/v) hydrochloric acid. To perform the assay, 0.1 ml of this solution along with 2 ml of HCl was added to 2 ml of the NO_x⁻-containing sample. The mixture was then heated in a boiling water bath for 5 min to enable diazotization, followed by cooling to ambient temperature. Subsequently, 0.2 ml of NEDA solution [1% (w/v) in 1% (v/v) HCl] was introduced, leading to the development of a colored azo dye. The samples were left at room temperature for 30 min, after which the absorbance of the developed chromophore was measured at 540 nm using a UV-vis spectrophotometer. Quantification was carried out by constructing a calibration curve with standard sodium nitrite (NaNO₂) solutions.

The Griess assay mentioned above was used specifically for the quantification of nitrite (NO₂⁻), as it selectively detects NO₂⁻, through the diazotization reaction forming an azo dye measurable at 540 nm. NO₃⁻ does not react directly in the Griess assay. Therefore, NO₃⁻ was first converted to NO₂⁻ using reduced form of nicotinamide adenine dinucleotide (NADH)–nitrate reductase method. NO₃⁻ concentrations were determined enzymatically using nitrate reductase with NADH as the electron donor. The reaction mixture contained the sample solution (prepared in 50 mM phosphate buffer, pH 7.5), 0.5 mM NADH, and 10 μ l of nitrate reductase solution per 1 ml of reaction mixture. The mixture was incubated at 30°C for 20 min to allow complete reduction of NO₃⁻ to NO₂⁻. After incubation, the generated NO₂⁻ was quantified using the Griess reaction.

Mass spectrometric quantification of NO₂⁻ and NO₃⁻

A 2 mM stock solution of NaNO₃ was prepared in HPLC-grade water and serially diluted to yield standard solutions of 1, 10, 50, 100, and 500 μ M. These standards were introduced into an LTQ mass spectrometer to establish a calibration curve. The product was scanned in the low mass range of *m/z* 20 to 100 in the negative ion mode. For each concentration, the total ion response was calculated from the intensity of NO₃⁻ (*m/z* 62). Normalized signal intensities were then plotted against concentration to generate the calibration curve, which was used to determine the NO₃⁻ concentrations in unknown samples. An analogous procedure was performed for NO₂⁻, where standard NaNO₂ solutions were used to obtain calibration curves based on the signal of NO₂⁻ (*m/z* 46).

Spectrophotometric and mass spectrometric analyses revealed that the NO_x⁻ concentrations determined by spectrophotometry are approximately close with the combined concentrations of NO₂⁻ and NO₃⁻ quantified by mass spectrometry.

$$[\text{NO}_x^-]_{\text{SP}} \sim \{[\text{NO}_2^-]_{\text{Mass}} + [\text{NO}_3^-]_{\text{Mass}}\}$$

Quantification of NO₂⁻ and NO₃⁻ using ion chromatography

The concentrations of NO₂⁻ and NO₃⁻ in aqueous samples were determined using a Dionex ICS-6000 ion chromatograph (Thermo Fisher Scientific) equipped with an IonPac AS11-HC anion-exchange column (4 \times 250 mm). Separation was achieved with a potassium hydroxide (KOH) gradient, starting at 5 mM for 5 min and increasing linearly to 20 mM over 25 min. The column temperature was maintained at 30°C, with a flow rate of 0.37 ml min⁻¹. Detection was performed using a suppressed conductivity detector. Calibration standards (1, 10, 50, 100, and 500 μ M) were prepared by serial dilution of sodium nitrite (NaNO₂) and sodium nitrate (NaNO₃) in ultrapure water. All samples were filtered through 0.22- μ m PTFE membrane filters before injection. Under the given parameters, NO₂⁻ eluted at approximately 6.2 min (retention time) and NO₃⁻ at 11.3 min. Peak identification was based on retention time matching with authentic standards. The concentrations of unknown samples were determined from calibration curve between peak area and standard concentration.

Quantification of ammonia

Two milliliters of the reaction sample was withdrawn from the reactor. To this, 2 ml of 1 M NaOH solution containing 5 wt % salicylic acid and 5 wt % sodium citrate was added. The mixture was then treated with 1 ml of 0.05 M NaClO and 0.2 ml of 1 wt % sodium nitroferrocyanide {Na₂[Fe(CN)₅NO]} solution. The mixture was allowed to stand for 30 min at room temperature to enable color development. In the presence of ammonia, the indophenol blue complex exhibits a characteristic absorption peak at 655 nm in the UV-vis spectrum.

Spin trap experiment

For spin trap studies, TEMPO was introduced into the aqueous Fe²⁺ solution at a final concentration of 400 μ g/ml (2.56 mM) before the nanobubbling experiment using air. After allowing the reaction to proceed for 1 hour, the samples were analyzed using an Orbitrap mass spectrometer equipped with a nanoESI source operated in positive ion mode at 1.6 kV. DMPO was used to capture NO and NO₂ generated in the solution.

Nanoparticle tracking analysis

NB size distribution and concentration were measured using a NanoSight NS300 equipped with a green laser and a scientific complementary metal-oxide semiconductor camera. The system was operated at 22 \pm 1°C. Each measurement consisted of five independent 60-s video captures from randomly selected regions of the sample cell. The viscosity was set to 1.0 cP, corresponding to pure water. The final reported size distribution and concentration represent the statistical average of all replicates, with standard errors included.

Zeta potential measurements

Zeta potential of NBs was determined using a Malvern Zetasizer Nano ZS (Malvern Instruments, UK) equipped with a 532-nm green laser and a modulator operating at 173° backscatter angle. Measurements were conducted in disposable folded capillary cells (DTS1070), previously rinsed thoroughly with ultrapure water. Each sample was allowed to equilibrate for 2 min before measurements. The dielectric constant, refractive index, and viscosity of the solvent were entered manually to ensure accurate Smoluchowski model-based zeta potential calculations. Each zeta potential value represents the mean of three independent measurements.

Supplementary Materials

This PDF file includes:

Supplementary Notes S1 to S3

Table S1

Figs. S1 to S29

REFERENCES

- O. Zayed, O. A. Hewedy, A. Abdelmoteleb, M. Ali, M. S. Youssef, A. F. Roumia, D. Seymour, Z.-C. Yuan, Nitrogen journey in plants: From uptake to metabolism, stress response, and microbe interaction. *Biomolecules* **13**, 1443 (2023).
- L. Camut, B. Gallova, L. Jilli, M. Sirlin-Josserand, E. Carrera, L. Sakvelidze-Achard, S. Ruffel, G. Krouk, S. G. Thomas, P. Hedden, A. L. Phillips, J.-M. Davière, P. Achard, Nitrate signaling promotes plant growth by upregulating gibberellin biosynthesis and destabilization of DELLA proteins. *Curr. Biol.* **31**, 4971–4982.e4 (2023).
- Exploring Nitric Acid (HNO₃): Properties, applications, & environmental impact; <https://alchemielabs.com/exploring-nitric-acid-hno3/?srsltid=AfmBOorYVsgarsPO9yNp8APer7N00Qh-80978xFOPEUNrLdtVEg9mS>.
- Nitric Acid Market Analysis: Industry Market Size, Plant Capacity, Production, Operating Efficiency, Demand & Supply, Type, End-User Industries, Sales Channel, Regional Demand, Foreign Trade, Company Share, 2015–2035; <https://www.chemanalyst.com/industry-report/nitric-acid-market-615>.
- US EPA, AP 42 Chapter 8.8 Nitric acid Production; <https://www3.epa.gov/ttnchie1/ap42/ch08/final/c08s08.pdf>.
- X. Zheng, H. Wu, Y. Gao, S. Chen, Y. Xue, Y. Li, Controllable assembly of highly oxidized cobalt on graphdiyne surface for efficient conversion of nitrogen into nitric acid. *Angew. Chemie Int. Ed.* **63**, e202316723 (2024).
- S. Han, C. Wang, Y. Wang, Y. Yu, B. Zhang, Electrosynthesis of nitrate via the oxidation of nitrogen on tensile-strained palladium porous nanosheets. *Angew. Chemie* **133**, 4524–4528 (2021).
- Y. Liu, M. Cheng, Z. He, B. Gu, C. Xiao, T. Zhou, Z. Guo, J. Liu, H. He, B. Ye, B. Pan, Y. Xie, Pothole-rich ultrathin WO₃ nanosheets that trigger N≡N bond activation of nitrogen for direct nitrate photosynthesis. *Angew. Chemie Int. Ed.* **58**, 731–735 (2019).
- P. Li, R. Li, Y. Liu, M. Xie, Z. Jin, G. Yu, Pulsed nitrate-to-ammonia electroreduction facilitated by tandem catalysis of nitrite intermediates. *J. Am. Chem. Soc.* **145**, 6471–6479 (2023).
- J. Zhang, B. Zhao, W. Liang, G. Zhou, Z. Liang, Y. Wang, J. Qu, Y. Sun, L. Jiang, Three-phase electrolysis by gold nanoparticle on hydrophobic interface for enhanced electrochemical nitrogen reduction reaction. *Adv. Sci.* **7**, 2002630 (2020).
- J. Zhang, S. Xia, Y. Wang, J. Wu, Y. Wu, Recent advances in dynamic reconstruction of electrocatalysts for carbon dioxide reduction. *iScience* **27**, 110005 (2024).
- X. Li, Y. Chen, Y. Tao, L. Shen, Z. Xu, Z. Bian, H. Li, Challenges of photocatalysis and their coping strategies. *Chem. Catal.* **2**, 1315–1345 (2022).
- M. Xiao, Z. Wang, K. Maeda, G. Liu, L. Wang, Addressing the stability challenge of photo(electro)catalysts towards solar water splitting. *Chem. Sci.* **14**, 3415–3427 (2023).
- K. Dong, Y. Yao, H. Li, H. Li, S. Sun, X. He, Y. Wang, Y. Luo, D. Zheng, Q. Liu, Q. Li, D. Ma, X. Sun, B. Tang, H₂O₂-mediated electrocatalysis of nitrate from air. *Nat. Synth.* **3**, 763–773 (2024).
- S. Chen, S. Liang, R. Huang, M. Zhang, Y. Song, Y. Zhang, S. Tao, L. Yu, D. Deng, Direct electroconversion of air to nitric acid under mild conditions. *Nat. Synth.* **3**, 76–84 (2024).
- W. Cao, Y. Li, B. Yan, Z. Zeng, P. Liu, R. Li, J. Jiang, Z. Ke, G. Yang, Catalyst-free activation and fixation of nitrogen by laser-induced conversion. *J. Am. Chem. Soc.* **146**, 14765–14775 (2024).
- J. K. Lee, K. L. Walker, H. S. Han, J. Kang, F. B. Prinz, R. M. Waymouth, H. G. Nam, R. N. Zare, Spontaneous generation of hydrogen peroxide from aqueous microdroplets. *Proc. Natl. Acad. Sci. U.S.A.* **116**, 19294–19298 (2019).
- M. A. Mehrgardi, M. Mofidfar, R. N. Zare, Sprayed water microdroplets are able to generate hydrogen peroxide spontaneously. *J. Am. Chem. Soc.* **144**, 7606–7609 (2022).
- X. Song, Y. Meng, R. N. Zare, Spraying water microdroplets containing 1,2,3-triazole converts carbon dioxide into formic acid. *J. Am. Chem. Soc.* **144**, 16744–16748 (2022).
- Z. Song, C. Zhu, K. Gong, R. Wang, J. Zhang, S. Zhao, Z. Li, X. Zhang, J. Xie, Deciphering the microdroplet acceleration factors of aza-michael addition reactions. *J. Am. Chem. Soc.* **146**, 10963–10972 (2024).
- X. Li, X. Nong, C. Zhu, X. Gao, H. Chen, X. Yuan, D. Xing, L. Liu, C. Liang, D. Zang, X. Zhang, Atomization by acoustic levitation facilitates contactless microdroplet reactions. *J. Am. Chem. Soc.* **146**, 29267–29271 (2024).
- B. K. Spoorthi, K. Debnath, P. Basuri, A. Nagar, U. V. Waghmare, T. Pradeep, Spontaneous weathering of natural minerals in charged water microdroplets forms nanomaterials. *Science* **384**, 1012–1017 (2024).
- X. Yan, R. M. Bain, R. G. Cooks, Organic reactions in microdroplets: Reaction acceleration revealed by mass spectrometry. *Angew. Chemie Int. Ed.* **55**, 12960–12972 (2016).
- Y. Meng, Y. Xia, J. Xu, R. N. Zare, Spraying of water microdroplets forms luminescence and causes chemical reactions in surrounding gas. *Sci. Adv.* **11**, eadt8979 (2025).
- J. Ghosh, R. G. Cooks, Mass spectrometry in materials synthesis. *TRAC Trends Anal. Chem.* **161**, 117010 (2023).
- A. Nandy, A. Kumar, S. Mondal, D. Koner, S. Banerjee, Spontaneous generation of aryl carbocations from phenols in aqueous microdroplets: Aromatic SN¹ reactions at the air–water interface. *J. Am. Chem. Soc.* **145**, 15674–15679 (2023).
- A. Nandy, S. Mondal, D. Koner, S. Banerjee, Heavy water microdroplet surface enriches the lighter isotopologue impurities. *J. Am. Chem. Soc.* **146**, 19050–19058 (2024).
- D. Satyabala, T. Ahuja, S. Bose, B. Mondal, P. Srikrishnarka, M. P. Kannan, B. K. Spoorthi, T. Pradeep, Transformation of nanodiamonds to onion-like carbons by ambient electrospray deposition. *J. Phys. Chem. C* **125**, 10998–11006 (2021).
- K. Naveen, S. Bose, C. Basheer, R. N. Zare, E. Gnanamani, Handheld portable device for delivering capped silver nanoparticles for antimicrobial applications. *QRB Discov.* **5**, e9 (2024).
- Y. Meng, E. Gnanamani, R. N. Zare, One-step formation of pharmaceuticals having a phenylacetic acid core using water microdroplets. *J. Am. Chem. Soc.* **145**, 7724–7728 (2023).
- S. Wang, S. Shan, S. Xiao, F. Liu, Z. Yang, S. Li, Z. Qiu, X. Dong, Y. Cheng, X. Zhang, Spontaneously generated electrons for CO₂ hydrogenation to formate at the microinterface of air–water. *Adv. Energy Mater.* **13**, 2303121 (2023).
- J. Dong, J. Chen, W. Wang, Z. Wei, Z.-Q. Tian, F. R. Fan, Charged microdroplets as microelectrochemical cells for CO₂ reduction and C–C coupling. *J. Am. Chem. Soc.* **146**, 2227–2236 (2024).
- G. Cassone, F. Saija, J. Sporer, S. Shaik, The reactivity-enhancing role of water clusters in ammonia aqueous solutions. *J. Phys. Chem. Lett.* **14**, 7808–7813 (2023).
- S. Bose, M. A. Mehrgardi, R. N. Zare, Selective photochemical conversion of carbon dioxide to formic acid at gas–water interface of microbubbles. *J. Am. Chem. Soc.* **147**, 27449–27457 (2025).
- S. Bose, M. Mofidfar, R. N. Zare, E. Gnanamani, Cross-coupling between arylboronic acids and terminal alkynes in water microdroplets. *J. Am. Chem. Soc.* **147**, 25779–25786 (2025).
- S. Bose, J. Xu, K. Lee, R. N. Zare, Catalyst-free production of urea from nitrate and carbon dioxide in water microdroplets. *Environ. Sci. Technol.* **59**, 10944–10954 (2025).
- S. Bose, R. N. Zare, Electric field-driven interfacial reduction of metal ions in microdroplets: Gold, silver, and nickel. *Chem. Sci.* **16**, 15455–15461 (2025).
- H. Xiong, J. K. Lee, R. N. Zare, W. Min, Strong electric field observed at the interface of aqueous microdroplets. *J. Phys. Chem. Lett.* **11**, 7423–7428 (2020).
- L. Shi, R. A. LaCour, N. Qian, J. P. Heindel, X. Lang, R. Zhao, T. Head-Gordon, W. Min, Water structure and electric fields at the interface of oil droplets. *Nature* **640**, 87–93 (2025).
- Z. Song, C. Liang, K. Gong, S. Zhao, X. Yuan, X. Zhang, J. Xie, Harnessing the high interfacial electric fields on water microdroplets to accelerate menshutkin reactions. *J. Am. Chem. Soc.* **145**, 26003–26008 (2023).
- H. Wei, E. P. Vejerano, W. Leng, Q. Huang, M. R. Willner, L. C. Marr, P. J. Vikesland, Aerosol microdroplets exhibit a stable pH gradient. *Proc. Natl. Acad. Sci. U.S.A.* **115**, 7272–7277 (2018).
- L. Qiu, Z. Wei, H. Nie, R. G. Cooks, Reaction acceleration promoted by partial solvation at the gas/solution interface. *ChemPlusChem* **86**, 1362–1365 (2021).
- K. R. Wilson, A. M. Prophet, G. Rovelli, M. D. Willis, R. J. Rapf, M. I. Jacobs, A kinetic description of how interfaces accelerate reactions in micro-compartments. *Chem. Sci.* **11**, 8533–8545 (2020).
- C. Zhu, L. N. Pham, X. Yuan, H. Ouyang, M. L. Coote, X. Zhang, High electric fields on water microdroplets catalyze spontaneous and fast reactions in halogen-bond complexes. *J. Am. Chem. Soc.* **145**, 21207–21212 (2023).
- A. C. Aragonès, N. L. Haworth, N. Darwish, S. Ciampi, E. J. Mannix, G. G. Wallace, I. Diez-Perez, M. L. Coote, Electrostatic catalysis of a Diels-Alder reaction. *Nature* **531**, 88–91 (2016).
- A. Kumar, V. S. Avadhani, A. Nandy, S. Mondal, B. Pathak, V. K. N. Pavuluri, M. M. Avulapati, S. Banerjee, Water microdroplets in air: A hitherto unnoticed natural source of nitrogen oxides. *Anal. Chem.* **96**, 10515–10523 (2024).
- Y. B. Vogel, C. W. Evans, M. Belotti, L. Xu, I. C. Russell, L.-J. Yu, A. K. K. Fung, N. S. Hill, N. Darwish, V. R. Gonçalves, M. L. Coote, K. Swaminathan Iyer, S. Ciampi, The corona of a surface bubble promotes electrochemical reactions. *Nat. Commun.* **11**, 6323 (2020).
- S. Bose, M. Mofidfar, R. N. Zare, Direct conversion of N₂ and air to nitric acid in gas–water microbubbles. *J. Am. Chem. Soc.* **146**, 27964–27971 (2024).
- S. Bose, Y. Xia, R. N. Zare, Understanding the formation of nitrate from nitrogen at the interface of gas–water microbubbles. *Chem. Sci.* **15**, 19764–19769 (2024).
- K. Lee, M. A. Mehrgardi, R. N. Zare, Interfacial curvature, not simply size, controls spontaneous hydrogen peroxide formation in water microdroplets. *J. Am. Chem. Soc.* **147**, 33240–33247 (2025).
- Y. Xia, X. Gao, J. Li, R. N. Zare, B. Chen, X. Zhang, Droplet-on-Demand Mass Spectrometry Reveals Curvature-Dependent Interfacial Reactivity in Aqueous Microdroplets, *Proc. Natl. Acad. Sci. U.S.A.* **122**, e2519491122 (2025).

52. D. Xing, Y. Meng, X. Yuan, S. Jin, X. Song, R. N. Zare, X. Zhang, Capture of hydroxyl radicals by hydronium cations in water microdroplets. *Angew. Chemie Int. Ed.* **61**, e202207587 (2022).
53. J. Li, Y. Xia, X. Song, B. Chen, R. N. Zare, Continuous ammonia synthesis from water and nitrogen via contact electrification. *Proc. Natl. Acad. Sci. U.S.A.* **121**, e2318408121 (2024).
54. S. F. Nami-Ana, M. A. Mehrgardi, M. Mofidfar, R. N. Zare, Sustained regeneration of hydrogen peroxide at the air–water interface of electrogenerated microbubbles on an electrode surface. *J. Am. Chem. Soc.* **146**, 31945–31949 (2024).
55. K. Lee, S. Bose, X. Song, S. Q. Choi, R. N. Zare, Continuous flow contact electrocatalysis for hydrogen peroxide production. *J. Phys. Chem. C* **129**, 6254–6261 (2025).
56. F. Li, J. Lv, A. He, J. Xu, L. Zhao, X. Wang, L. Mao, S. Li, H. Wang, Y. Wang, G. Jiang, Unexpected generation of singlet oxygen at the air–water interface of aqueous microdroplets. *J. Am. Chem. Soc.* **147**, 30574–30581 (2025).
57. M. Angelaki, J. d'Erceville, D. J. Donaldson, C. George, pH affects the spontaneous formation of H₂O₂ at the air–water interfaces. *J. Am. Chem. Soc.* **146**, 25889–25893 (2024).
58. X. Song, Y. Wan, Q. Yang, J. Zhang, Y. Zhang, Z. Sun, S. Li, J. Zhang, X. Zhang, S. Ciampi, L. Zhang, Electrode fouling by gas bubbles enables catalyst-free hydrogen peroxide synthesis. *J. Am. Chem. Soc.* **147**, 22864–22872 (2025).
59. T. Li, S. Han, C. Wang, Y. Huang, Y. Wang, Y. Yu, B. Zhang, Ru-doped Pd nanoparticles for nitrogen electrooxidation to nitrate. *ACS Catal.* **11**, 14032–14037 (2021).
60. Y. Guo, S. Zhang, R. Zhang, D. Wang, D. Zhu, X. Wang, D. Xiao, N. Li, Y. Zhao, Z. Huang, W. Xu, S. Chen, L. Song, J. Fan, Q. Chen, C. Zhi, Electrochemical nitrate production via nitrogen oxidation with atomically dispersed Fe on N-doped carbon nanosheets. *ACS Nano* **16**, 655–663 (2022).
61. Z. Wang, Q. Zhang, H. Wang, C. Sun, X. Li, H. He, J. Wang, Y. Zhao, X. Zhang, Efficient nitrate generation through electrochemical N₂ oxidation with nickel oxyhydroxide decorated copper hydroxide driven by solar cells. *Small* **19**, 2301438 (2023).
62. H. Song, X. Liu, L. Zhang, X. Zhang, H. Yu, X. Yang, M. Guo, Z. Liang, X. Lin, X. Liu, X. Ding, Two orders of magnitude enhancement in nitrogen oxidation via H₂SO₄-mediated Fe-TiO₂ electrocatalysis. *ACS Nano* **19**, 21858–21865 (2025).
63. Y. Liu, Y. Cheng, S. Ye, J. Hong, W. Lin, Insights into oxygen vacancy-enhanced WO₃ nanosheets for electrocatalytic nitrogen oxidation to nitrate. *New J. Chem.* **49**, 18249–18253 (2025).
64. C. Dai, Y. Sun, G. Chen, A. C. Fisher, Z. J. Xu, Electrochemical oxidation of nitrogen towards direct nitrate production on spinel oxides. *Angew. Chemie Int. Ed.* **59**, 9418–9422 (2020).
65. M. Kuang, Y. Wang, W. Fang, H. Tan, M. Chen, J. Yao, C. Liu, J. Xu, K. Zhou, Q. Yan, Efficient nitrate synthesis via ambient nitrogen oxidation with Ru-doped TiO₂/RuO₂ electrocatalysts. *Adv. Mater.* **32**, 2002189 (2020).
66. L. Zhang, M. Cong, X. Ding, Y. Jin, F. Xu, Y. Wang, L. Chen, L. Zhang, A Janus Fe–SnO₂ catalyst that enables bifunctional electrochemical nitrogen fixation. *Angew. Chemie Int. Ed.* **59**, 10888–10893 (2020).
67. J. Yang, Z. Ruan, S. Jiang, P. Xia, Q. Yang, Q. Zhang, C. Xiao, Y. Xie, Ce-doped W₁₈O₄₉ nanowires for tuning N₂ activation toward direct nitrate photosynthesis. *J. Phys. Chem. Lett.* **12**, 11295–11302 (2021).
68. S. Shao, J. Zhang, L. Li, Y. Qin, Z.-Q. Liu, T. Wang, Visible-light-driven photocatalytic N₂ fixation to nitrates by 2D/2D ultrathin BiVO₄ nanosheet/rGO nanocomposites. *Chem. Commun.* **58**, 2184–2187 (2022).
69. X. Deng, P. Chen, R. Cui, X. Gong, Y. Wu, X. Wang, C. Deng, Dynamic reconfiguration and local polarization of NiFe-layered double hydroxide–Bi₂MoO_{6-x} heterojunction for enhancing piezo-photocatalytic nitrogen oxidation to nitric acid. *Adv. Sci.* **11**, 2401667 (2024).
70. P. Xia, X. Pan, S. Jiang, J. Yu, B. He, P. M. Ismail, W. Bai, J. Yang, L. Yang, H. Zhang, M. Cheng, H. Li, Q. Zhang, C. Xiao, Y. Xie, Designing a redox heterojunction for photocatalytic “overall nitrogen fixation” under mild conditions. *Adv. Mater.* **34**, 2200563 (2022).
71. S. M. Montazeri, N. Kalogerakis, G. Kollopoulos, Effect of chemical species and temperature on the stability of air nanobubbles. *Sci. Rep.* **13**, 16716 (2023).
72. M. Karimi, G. Parsafar, H. Samouei, Polarizing perspectives: Ion- and dipole-induced dipole interactions dictate bulk nanobubble stability. *J. Phys. Chem. B* **128**, 7263–7270 (2024).
73. M. Alheshibri, J. Qian, M. Jehannin, V. S. J. Craig, A history of nanobubbles. *Langmuir* **32**, 11086–11100 (2016).
74. S. Wang, L. Zhou, Y. Gao, Can bulk nanobubbles be stabilized by electrostatic interaction? *Phys. Chem. Chem. Phys.* **23**, 16501–16505 (2021).
75. S. I. Koshoridze, Y. K. Levin, Comment on “Can bulk nanobubbles be stabilized by electrostatic interaction?” by S. Wang, L. Zhou and Y. Gao. *Phys. Chem. Chem. Phys.*, 2021, 23, 16501. *Phys. Chem. Chem. Phys.* **24**, 10622–10625 (2022).
76. N. Nirmalkar, A. W. Pacey, M. Barigou, Interpreting the interfacial and colloidal stability of bulk nanobubbles. *Soft Matter* **14**, 9643–9656 (2018).
77. J. N. Meegoda, S. A. Hewage, J. H. Batagoda, Application of the diffused double layer theory to nanobubbles. *Langmuir* **35**, 12100–12112 (2019).
78. F. Collin, Chemical basis of reactive oxygen species reactivity and involvement in neurodegenerative diseases. *Int. J. Mol. Sci.* **20**, 2407 (2019).
79. S. Shen, R. Chen, X. Li, J. Wang, S. Yu, J. Li, F. Dong, Regulating the selectivity of nitrate photoreduction for purification or ammonia production by cooperating oxidative half-reactions. *Environ. Sci. Technol.* **58**, 7653–7661 (2024).
80. R. Zhang, Y. Zhang, B. Xiao, S. Zhang, Y. Wang, H. Cui, C. Li, Y. Hou, Y. Guo, T. Yang, J. Fan, C. Zhi, Phase engineering of high-entropy alloy for enhanced electrocatalytic nitrate reduction to ammonia. *Angew. Chemie Int. Ed.* **63**, e202407589 (2024).
81. H. J. Li, T. Zhu, D. F. Zhao, Z. F. Zhang, Z. M. Chen, Kinetics and mechanisms of heterogeneous reaction of NO₂ on CaCO₃ surfaces under dry and wet conditions. *Atmos. Chem. Phys.* **10**, 463–474 (2010).
82. H. Kojima, N. Nakatsubo, K. Kikuchi, S. Kawahara, Y. Kirino, H. Nagoshi, Y. Hirata, T. Nagano, Detection and imaging of nitric oxide with novel fluorescent indicators: Diaminofluoresceins. *Anal. Chem.* **70**, 2446–2453 (1998).
83. J. L. Parker, S. Newstead, Molecular basis of nitrate uptake by the plant nitrate transporter NRT1.1. *Nature* **507**, 68–72 (2014).
84. N. Xu, L. Cheng, Y. Kong, G. Chen, L. Zhao, F. Liu, Functional analyses of the NRT2 family of nitrate transporters in *Arabidopsis*. *Front. Plant Sci.* **15**, 1351998 (2024).
85. N. Gnayem, R. Unis, R. Gnaim, A. Chemodanov, A. Israel, J. Gnaim, A. Golberg, Fatty acid content and profile in *Ulva lactuca* in response to exposure to variable growth conditions in indoor photobioreactors. *Life (Basel)* **15**, 57 (2025).
86. K. L. Van Alstyne, Seawater nitrogen concentration and light independently alter performance, growth, and resource allocation in the bloom-forming seaweeds *Ulva lactuca* and *Ulvaria obscura* (Chlorophyta). *Harmful Algae* **78**, 27–35 (2018).
87. Why Nitrate is the Most Efficient N Source; <https://www.yara.us/crop-nutrition/nitrate-is-the-most-efficient-nitrogen-source/>.
88. C. Muratore, L. Espen, B. Prinsi, Nitrogen uptake in plants: The plasma membrane root transport systems from a physiological and proteomic perspective. *Plants* **10**, 681 (2021).

Acknowledgments: We thank Stanford Soft & Hybrid Materials Facility (SMF) for providing access to the equipment for analysis. **Funding:** S.B. thank the Nehru-Fulbright program (grant number: 2984/FNPDR/2023) for the fellowship. We thank the Air Force Office of Scientific Research through the Multidisciplinary University Research Initiative (MURI) program (AFOSR FA9550-21-1-0170) for supporting this project. **Author contributions:** Conceptualization: S.Bo., S.Ba., H.S., and R.N.Z. Methodology: S.Bo., S.Ba., Y.H., H.S., and R.N.Z. Investigation: S.Bo., S.Ba., Y.H., and H.S. Visualization: S.Bo., H.S., and R.N.Z. Funding acquisition: S.Bo. and R.N.Z. Supervision: H.S. and R.N.Z. Writing—original draft: S.Bo. and H.S. Writing—review and editing: S.Bo., H.S., and R.N.Z. Resources: S.Bo., H.S., and R.N.Z. Project administration: S.Bo., H.S., and R.N.Z. Validation: S.Bo., H.S., and R.N.Z. **Competing interests:** The authors declare that they have no competing interests. **Data and materials availability:** All data and code needed to evaluate and reproduce the results in the paper are present in the paper and/or the Supplementary Materials. This study did not generate new materials.

Submitted 18 September 2025

Accepted 5 January 2026

Published 6 February 2026

10.1126/sciadv.aec4225

Highly efficient production of nitrite and nitrate from air at the gas-water interface of nanobubbles

Sandeep Bose, Saeed Bahadorikhalili, Yuanyi He, Hamidreza Samouei, and Richard N. Zare

Sci. Adv. **12** (6), eaec4225. DOI: 10.1126/sciadv.aec4225

View the article online

<https://www.science.org/doi/10.1126/sciadv.aec4225>

Permissions

<https://www.science.org/help/reprints-and-permissions>

Use of this article is subject to the [Terms of service](#)

Science Advances (ISSN 2375-2548) is published by the American Association for the Advancement of Science, 1200 New York Avenue NW, Washington, DC 20005. The title *Science Advances* is a registered trademark of AAAS.

Copyright © 2026 The Authors, some rights reserved; exclusive licensee American Association for the Advancement of Science. No claim to original U.S. Government Works. Distributed under a Creative Commons Attribution NonCommercial License 4.0 (CC BY-NC).